Doctoral Dissertation

Studies on Novel Catalysts for Direct Decomposition of Nitrous Oxide Based on Rare Earth Oxides with C-type Structure

(立方晶 C 型構造を有する希土類酸化物を母体とした
新規な亜酸化窒素直接分解触媒に関する研究)

Chang-Min Cho

December 2019

Department of Applied Chemistry
Graduate School of Engineering
Osaka University

Studies on Novel Catalysts for Direct Decomposition of Nitrous Oxide Based on Rare Earth Oxides with C-type Structure

(立方晶 C 型構造を有する希土類酸化物を母体とした
新規な亜酸化窒素直接分解触媒に関する研究)

Chang-Min Cho

December 2019

Department of Applied Chemistry
Graduate School of Engineering
Osaka University

Preface

The work of this thesis has been carried out under the supervision of Professor Dr. Nobuhito Imanaka at Department of Applied Chemistry, Graduate School of Engineering, Osaka University.

The object of this thesis is to develop novel catalysts for direct decomposition of nitrous oxide using cubic C-type structure of rare earth sesquioxides, R_2O_3 (R: rare earth).

The author wishes that the findings and the knowledge obtained in this work will provide useful information for further development and design of catalyst for the decomposition of nitrous oxide and that the materials would contribute to practical applications.

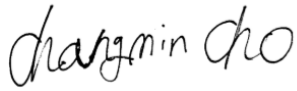

Chang-Min Cho

Department of Applied Chemistry

Graduate School of Engineering

Osaka University

2-1 Yamadaoka, Suita, Osaka 565-0871,

Japan

December 2019

Contents

General Introduction

Nitrous oxide (N_2O) is a highly potent greenhouse effect gas, and its global warming potential is ca. 300 times higher than that of carbon dioxide. N_2O also destroys the ozone layer in the stratosphere, similar to chlorofluorocarbons [1]. In addition, N_2O molecule is thermodynamically stable, whose lifetime is ca. 150 years in the atmosphere. In industrial settings, N_2O is emitted as by-product in the chemical process of such as nitric acid and adipic acid, and the atmospheric N_2O concentration has rapidly increased during past several decades [2]. To prevent global warming and ozone layer depletion, therefore, it is highly required to reduce N_2O gas into the atmosphere.

Several methods for the effective N_2O decomposition are proposed, such as selective catalytic reduction (SCR) with NH_3 [3, 4], thermal decomposition [5, 6], and direct catalytic decomposition [7, 8]. The SCR method with NH_3 achieves the efficient reduction of N_2O to N_2 and H_2O by using SCR catalysts such as Fe-zeolite with NH_3 as reductant [3]. However, this method requires an additional equipment to supply the NH_3 gas, and the secure control systems is indispensable due to the high toxicity, flammability, and corrosiveness of NH_3 [9]. For the thermal decomposition method, N_2O is decomposed into N_2 and O_2 gases without reducing additives at temperatures higher than 800 °C. However, such elevated temperatures cause a deterioration of heating systems. On the other hand, the direct catalytic decomposition of N_2O into N_2 and O_2 gases is accepted as an ideal route for N_2O abatement, because the operation temperature is lower than that for the thermal decomposition method and reducing additives are not needed [10]. As the direct N_2O decomposition catalysts, noble metal-based catalysts such as Pt/Al_2O_3 [11] and Pd/Al_2O_3 [12] have been reported to exhibit the satisfactory activity, while the high cost and the scarce resource of noble metals restrict their widespread industrial application. Therefore, noble metal-free catalysts have been extensively studied, and the effective N_2O decomposition activities were reported for zeolites (Co-ZSM5, Fe-ZSM5, etc.)

[13, 14], spinel-type oxides (Co_3O_4, $Zn_xCo_{1-x}Co_2O_4$, $Ni_xCo_{1-x}Co_2O_4$, etc.) [15, 16], and perovskite-type oxides ($Pr_{1-x}Ba_xMnO_3$, $La_{1-x}Sr_xFeO_3$, etc.) [17, 18]. However, zeolites lack the thermal stability over 500 °C, and spinel-type and perovskite-type oxides are deactivated by the presence of O_2, CO_2, or water vapor [19-23].

According to the previous studies, the direct N_2O decomposition is proceeded by the following steps. [2, 24, 25]. Gaseous N_2O is adsorbed on the active site (labeled * in **eq. G-1**), and then, the N-O bond is cleaved, resulting in the formation of N_2 gas and adsorbed oxygen species (O*, **eq. G-2**). The O* species are subsequently removed as O_2 gas by the recombination of two adjacent O* (**eq. G-3**) or by directly reacted with N_2O (**eq. G-4**). In this mechanism, the formation and/or control of active site of the catalyst is important issue for the N_2O decomposition.

$$N_2O + * \rightarrow N_2O* \quad \text{(G-1)}$$

$$N_2O* \rightarrow N_2 + O* \quad \text{(G-2)}$$

$$2O* \rightarrow O_2 + 2* \quad \text{(G-3)}$$

$$O* + N_2O \rightarrow N_2 + O_2 + * \quad \text{(G-4)}$$

The aim of this doctoral thesis is to develop novel catalysts effective for the direct N_2O decomposition with high thermal stability and high durability for co-existing gas. To this end, rare earth sesquioxides, R_2O_3 (R: rare earths), were focused as the base material of novel catalysts for the direct N_2O decomposition. R_2O_3 are thermally stable oxides whose melting points are over 2200 °C, and have three kinds of crystal polymorphs depending on the temperature and the ionic-size of the rare earth elements; i.e., hexagonal A-type ($P\bar{3}m1$), monoclinic B-type ($C2/m$), and cubic C-type ($Ia\bar{3}$), as shown in **Figure G-1** [26]. In the hexagonal A-type R_2O_3 which is generally obtained for the oxides containing large rare earths, the R^{3+} cation holds a coordination number of 7; four O^{2-} anions are closer than the other three O^{2-} anions. With decreasing the cationic radius of rare earth, the structure of R_2O_3 transformed to the monoclinic B-type structure which is formed by a distortion of the A-type structure. In the B-type structure, the R^{3+} cation can hold six- and seven coordination numbers. The

cubic C-type structure is related to the doubled-edge fluorite-type structure (**Figure G-1**) with one-quarter of the oxide anion sites vacant; i.e., the C-type structure possesses regularly ordered oxide ion vacancy sites, resulting in the six-coordination of R^{3+} site. As shown in **Figure G-2**, the lattice volume of the C-type structure is larger than those of the A-type and B-type structures, and it has been reported that the C-type structure possesses large open spaces derived from the oxide ion vacancy and the large lattice volume. These open spaces are expected to work as adsorption and active sites for the direct N_2O decomposition.

This thesis consists of the following three chapters.

To develop the novel catalysts for N_2O decomposition, various kinds of fine C-type rare earth oxides, R_2O_3 (R = Y, Eu, Gd, Dy, Ho, Er, Tm, Yb, and Lu), were synthesized by a co-precipitation method, and in **chapter 1**, their N_2O decomposition activities are described. Moreover, since the acceleration of the removal of adsorbed oxygen, which is regarded as rate-determining, is essential for realizing high N_2O decomposition activity, I introduced $Pr^{3+/4+}$ into the Yb_2O_3 lattice to give the redox properties. Furthermore, $Co^{2+/3+}$ ions were doped into the Yb_2O_3 lattice to produce an additional oxide ion vacancy, which is expected to be an active site for N_2O decomposition, in the structure as well as giving the redox property. Thus, Yb_2O_3-Pr_6O_{11} and Yb_2O_3-Co_3O_4 solid solutions were synthesized and investigated their catalytic activities for the direct N_2O decomposition.

In **chapter 2**, the contribution of oxide ion vacancy in the cubic C-type structure to the N_2O decomposition ability is described. I synthesized ZrO_2-Y_2O_3 solid solutions, where they can form fluorite-type or cubic C-type structure depending on their compositions, and discussed the effect of the oxide ion vacancy on the catalytic activity.

Chapter 3 deals with the effects of the redox property and oxide ion vacancy on the direct N_2O decomposition activity. To discuss them in detail, the Yb_2O_3-MO_x (M = Pr, Co, Cu, Sr, Zr) solid solutions were prepared by doping various kinds of cations. Here, $Pr^{3+/4+}$, $Co^{2+/3+}$, and $Cu^{+/2+}$ ions were selected to give the redox properties. The substitution of low-valent Co^{2+}, $Cu^{+/2+}$, or Sr^{2+} in the

Yb^{3+} sites can form the oxide ion vacancies. Conversely, the introduction of high-valent Pr^{4+} or Zr^{4+} intentionally decreases the oxide ion vacancies in the C-type structure. For these concepts, the N_2O decomposition activities in the Yb_2O_3-MO_x (M = Pr, Co, Cu, Sr, Zr) solids were compared, and the effects of the redox properties and the oxide ion vacancy on the activity were discussed.

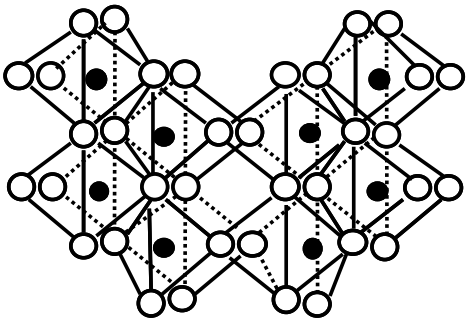

A-type hexagonal

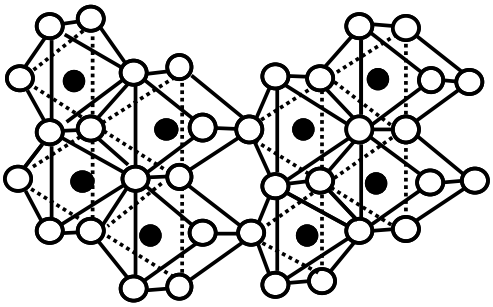

B-type monoclinic

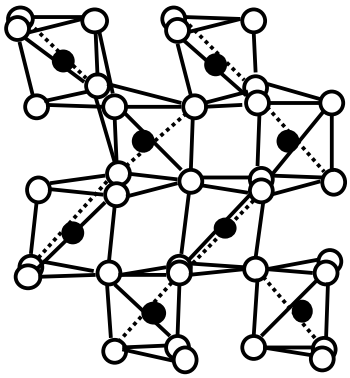

C-type cubic

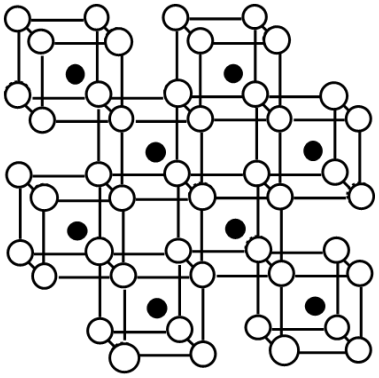

Fluorite-type

Figure G-1 Crystal structures of A-, B-, and C-type R_2O_3 and fluorite-type RO_2. The closed and open circles indicate the rare earth cation and oxide anion, respectively.

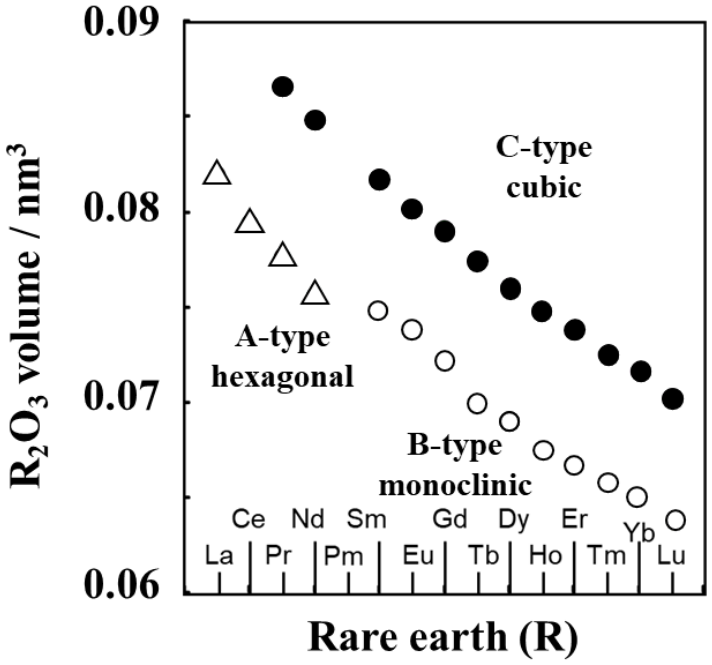

Figure G-2 Lattice volume of rare earth sesquioxides.

List of Publications

1. Direct Decomposition of Nitrous Oxide Using Yb_2O_3-Pr_6O_{11} with C-type Cubic Structure

   Chang-Min Cho, Yuka Watanabe, Naoyoshi Nunotani, Nobuhito Imanaka

   Chemistry Letters, 2018, **47**, 996-999.

2. Direct Decomposition of N_2O over C-type Cubic Yb_2O_3-Co_3O_4 Catalysts

   Chang-Min Cho, Naoyoshi Nunotani, Nobuhito Imanaka

   Bulletin of the Chemical Society of Japan, 2019, **92**, 1148-1153.

3. Effect of Oxygen Vacancies on Direct N_2O Decomposition over ZrO_2-Y_2O_3 Catalysts

   Chang-Min Cho, Naoyoshi Nunotani, Nobuhito Imanaka

   J. Asian Ceram. Soc., in press.

4. Effect of Introducing MO_x (M = Sr, Zr, Cu, Co, Pr) into C-type Yb_2O_3 on Direct N_2O Decomposition Activity

   Chang-Min Cho, Naoyoshi Nunotani, Nobuhito Imanaka

   in preparation.

Chapter 1

Direct N_2O Decomposition Using Rare Earth Oxide with C-type Structure

1.1. Introduction

As mentioned in the General Introduction, cubic C-type rare earth oxides (R_2O_3) are expected to facilitate N_2O decomposition, because C-type structure possesses large interstitial open spaces derived by removed one-quarter of the oxide ions from the fluorite-type structure. Therefore, I selected cubic C-type R_2O_3 as the mother solid of the catalyst. To obtain a catalyst realizing the high N_2O decomposition activity, it is essential to select the C-type R_2O_3 having enough N_2O decomposition activity and modify its catalytic activity by introducing another cation into the R_2O_3 lattice to improve redox and/or adsorption/desorption properties which strongly affect the steps of N_2O decomposition on the catalyst (**eqs. G1-G4**).

For discussing the N_2O decomposition activity of the mother solid of R_2O_3 strictly, the C-type R_2O_3 (R = Y, Eu, Gd, Dy, Ho, Er, Tm, Yb, and Lu) were prepared from $R(NO_3)_3$ aqueous solution. Moreover, I selected $Pr^{3+/4+}$ and $Co^{2+/3+}$ as the dopant cations into the Yb_2O_3, which showed the highest N_2O decomposition activity among the prepared R_2O_3. The $Pr^{3+/4+}$ doping into the Yb_2O_3 lattice gives a redox ability caused by the valence change of $Pr^{3+/4+}$ ions, which should facilitate the removal of adsorbed oxygen. For the doping of $Co^{2+/3+}$ to the Yb^{3+} site of Yb_2O_3, both the redox property and the generation of oxide ion vacancy are simultaneously realized. The generated oxide ion vacancies may work as additional active sites for the N_2O decomposition. Therefore, the $(Yb_{1-x}Pr_x)_2O_{3+\delta}$ and the $(Yb_{1-x}Co_x)_2O_{3-\delta}$ solids were prepared and the catalytic activities were investigated.

1.2. Experimental Procedure

Fine rare earth sesquioxides, R_2O_3 (R = Y, Eu, Gd, Dy, Ho, Er, Tm, Yb, and Lu), were synthesized via a co-precipitation method. 1 mol·L^{-1} $R(NO_3)_3$ (R = Y, Eu, Gd, Dy, Ho, Er, Tm, Yb, and Lu) aqueous solution was added into a 1 mol·L^{-1} $(NH_4)_2CO_3$ aqueous solution and stirred vigorously. The pH value of the mixed solution was adjusted to 9 by dropwise addition of 4 mol·L^{-1} ammonia aqueous solution to obtain a precipitation. After stirring the solution for 6 h at room temperature, the precipitation was recovered by suction filtration, dried, and then calcined at 500 °C for 6 h in air. The $(Yb_{1-x}M_x)_2O_{3-\delta}$ (M = Pr, Co) solids were also obtained via a co-precipitation method using 1 mol·L^{-1} $Yb(NO_3)_3$ and 1 mol·L^{-1} $Pr(NO_3)_3$ or $Co(NO_3)_2$ aqueous solutions as starting materials by similar manner.

The sample compositions were determined by X-ray fluorescence spectrometry (XRF; Supermini200, Rigaku) and the crystal structures of the samples were identified by X-ray powder diffraction (XRD; SmartLab, Rigaku) analysis with Cu-Kα radiation (40 kV and 30 mA). The lattice constants were calculated by refining the XRD peak angles using α-Al_2O_3 as an internal standard. The specific surface areas of catalysts were measured by the Brunauer-Emmett-Teller (BET) method using nitrogen adsorption at −196 °C (TriStar 3000, Micromeritics).

The catalytic activities for the N_2O direct decomposition were investigated using a conventional fixed-bed flow reactor with a 10 mm diameter quartz glass tube. **Figure 1-1** illustrates a schematic view of the equipment used for the activity test. A gas mixture of 0.5 vol% N_2O-99.5 vol% He was fed at a flow rate of 60 mL·min^{-1} over 0.2 g of catalyst, where the *W*/*F* ratio (*W*: catalyst weight, *F*: gas flow rate) was 0.2 g·s·mL^{-1}. Prior to the catalytic activity tests, each catalyst was preheated at 200 °C for 1 h under a He flow to remove adsorbed water on surface. After the reaction, the gas composition was analyzed by a thermal conductivity detection type gas chromatography (GC-8AIT,

Shimadzu). The resultant gas was also analyzed by gas chromatograph mass spectrometry (GCMS; GCMS-QP2010 Plus; Shimadzu) to identify the product formed after N_2O decomposition.

The influence of the presence of O_2, CO_2, and water vapor on the N_2O decomposition was investigated by flowing the 0.5 vol% N_2O (He valance) mixed with various concentration of O_2, CO_2 or water vapor, where the total flow rate was kept constant at 60 $mL \cdot min^{-1}$.

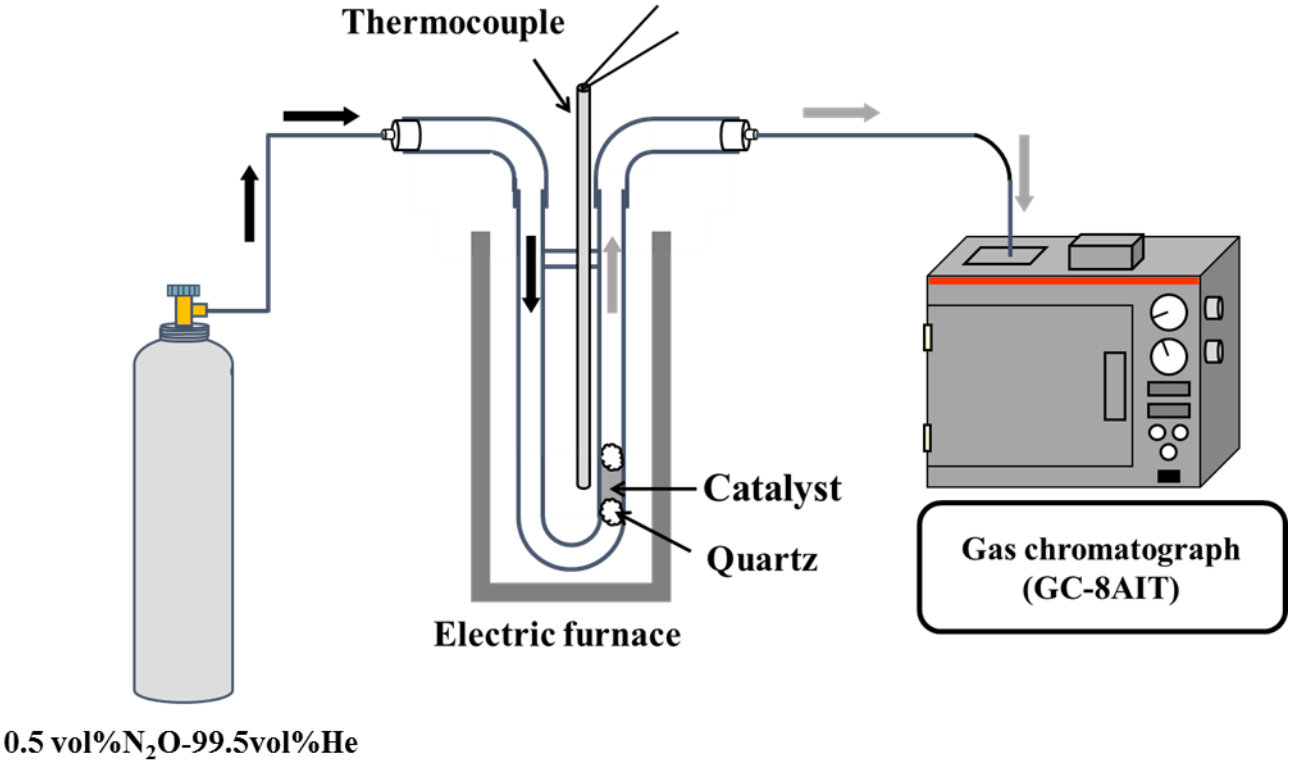

Figure 1-1 A schematic view of the fixed-bed flow reactor for the direct N_2O decomposition.

1.3. Results and Discussion

1.3.1. R_2O_3 (R = Y, Eu, Gd, Dy, Ho, Er, Tm, Yb, and Lu) catalysts

Figure 1-2 shows the XRD patterns of R_2O_3 (R = Y, Eu, Gd, Dy, Ho, Er, Tm, Yb, and Lu) obtained by the co-precipitation method. All samples possessed the single phase of cubic C-type rare earth sesquioxide structure. BET surface areas and N_2O conversion at 500 °C of the R_2O_3 samples are listed in **Table 1-1**. Among the samples, Yb_2O_3 exhibited the highest catalytic activity. The reason why the highest catalytic activity was obtained for Yb_2O_3 is considered to be due to the comparatively large surface area and the redox property of Yb ($Yb^{2+/3+}$). From this result, the Yb_2O_3 was selected as the mother solid of the present catalyst.

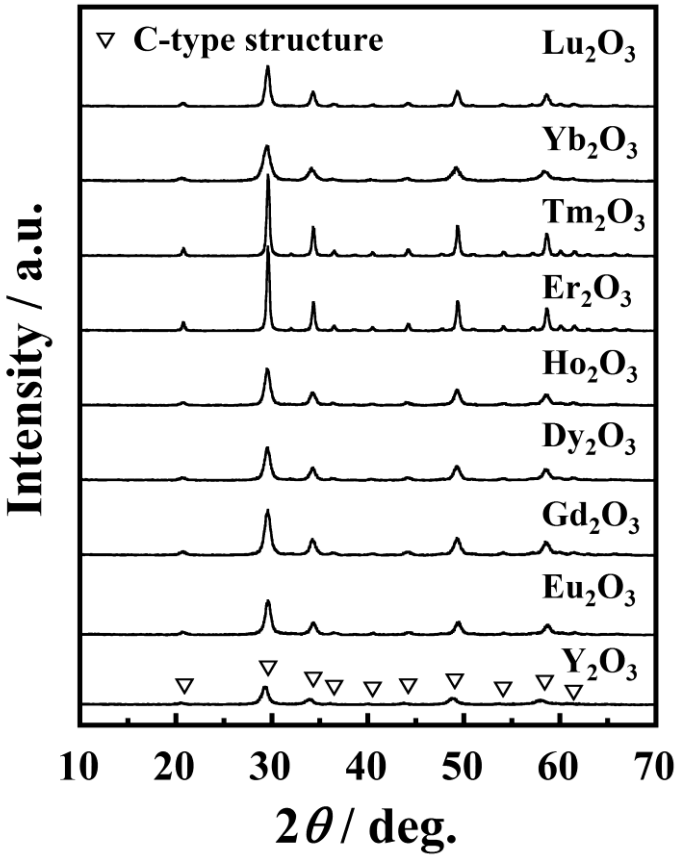

Figure 1-2 XRD patterns of R_2O_3 (R = Y, Eu, Gd, Dy, Ho, Er, Tm, Yb, and Lu).

Table 1-1 Surface area and N_2O conversion at 500 °C of R_2O_3 (R = Y, Eu, Gd, Dy, Ho, Er, Tm, Yb, and Lu)

Catalyst	Surface area / $m^2 \cdot g^{-1}$	N_2O conversion / %
Y_2O_3	49.6	81.1
Eu_2O_3	42.6	79.1
Gd_2O_3	48.4	68.2
Dy_2O_3	43.6	76.8
Ho_2O_3	43.7	61.7
Er_2O_3	41.7	83.4
Tm_2O_3	61.1	77.8
Yb_2O_3	50.0	88.8
Lu_2O_3	48.3	75.5

1.3.2. Yb_2O_3-Pr_6O_{11} catalysts

The compositions measured by XRF and the BET specific surface areas of the $(Yb_{1-x}Pr_x)_2O_{3+\delta}$ catalysts are summarized in **Table 1-2**. The measured compositions of the catalysts were in good agreement with their stoichiometric values within experimental errors. For the surface area, a substantial decrease was observed with increasing Pr content, because the introduction of $Pr^{3+/4+}$ ions may induce particle aggregation.

Figure 1-3 shows the XRD patterns of the $(Yb_{1-x}Pr_x)_2O_{3+\delta}$ catalysts. For the samples with $x \leq 0.15$, the patterns clearly indicate the formation of the crystalline phase having the C-type structure without any crystalline impurities. For the sample with $x = 0.20$, an additional Pr_6O_{11} phase was appeared. The lattice constant of the C-type structure is also shown in **Table 1-2**. Lattice expansion was observed with increasing the Pr content up to $x = 0.15$ due to the replacement of the Yb^{3+} ion (0.101 nm [coordination number (CN) = 6] [27]) site by larger Pr^{3+} ion (0.113 nm [CN = 6] [27]), while Pr^{4+} holds slightly smaller ionic-size (0.099 nm [CN = 6] [27]) than the Yb^{3+} ion. The lattice

constant of the sample with $x = 0.20$ was almost the same as the $x = 0.15$ sample. Therefore, it can be determined the solid solubility limit composition is $x = 0.15$.

Table 1-2 Composition measured by XRF, BET surface area, and lattice constant of $(Yb_{1-x}Pr_x)_2O_{3+\delta}$

Catalyst	Measured composition	Surface area / $m^2 \cdot g^{-1}$	Lattice constant / nm
Yb_2O_3	Yb_2O_3	50.0	1.0461
$(Yb_{0.95}Pr_{0.05})_2O_{3+\delta}$	$(Yb_{0.95}Pr_{0.05})_2O_{3+\delta}$	40.2	1.0475
$(Yb_{0.90}Pr_{0.10})_2O_{3+\delta}$	$(Yb_{0.90}Pr_{0.10})_2O_{3+\delta}$	35.9	1.0492
$(Yb_{0.85}Pr_{0.15})_2O_{3+\delta}$	$(Yb_{0.86}Pr_{0.14})_2O_{3+\delta}$	32.1	1.0510
$(Yb_{0.80}Pr_{0.20})_2O_{3+\delta}$	$(Yb_{0.79}Pr_{0.21})_2O_{3+\delta}$	33.3	1.0511

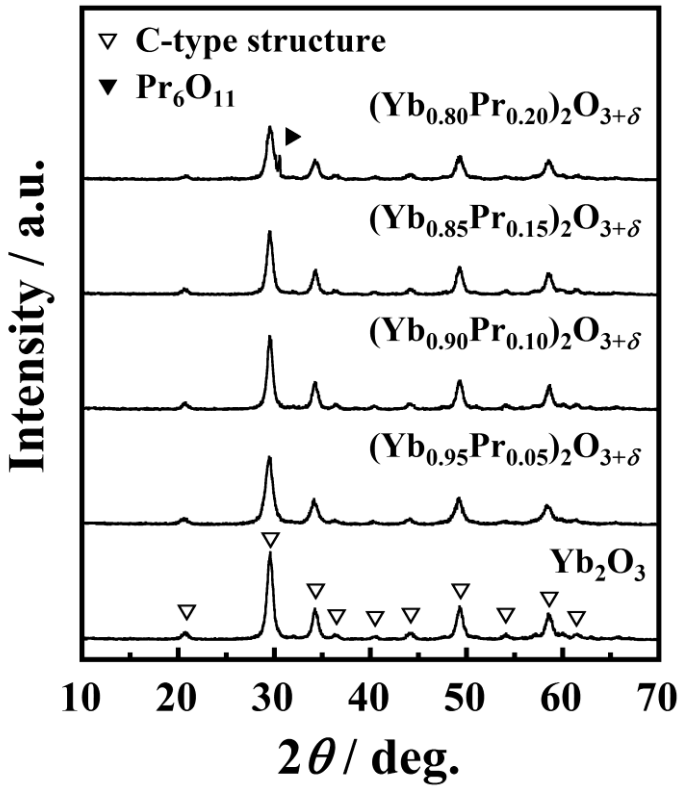

Figure 1-3 XRD patterns of $(Yb_{1-x}Pr_x)_2O_{3+\delta}$.

Figure 1-4 displays the temperature dependencies of the N_2O decomposition activity for the $(Yb_{1-x}Pr_x)_2O_{3+\delta}$ catalysts. For the catalysts with $x \leq 0.15$, the N_2O decomposition activity increased with increasing the Pr content (x), even though the surface areas of the Pr-doped samples were lower than that of Yb_2O_3. In the case of $(Yb_{1-x}Pr_x)_2O_{3+\delta}$ (x = 0.10, 0.15, 0.20), the complete N_2O decomposition was achieved at 500 °C. It is noticed that the N_2O was completely decomposed to N_2 and O_2 without formation of any gas species. The improvement in activity is attributed to the increase of the redox property of the solid caused by the existence of $Pr^{3+/4+}$ ions, and the highest activity was obtained for the $(Yb_{0.85}Pr_{0.15})_2O_{3+\delta}$ (x = 0.15) solid. The activity of $(Yb_{0.80}Pr_{0.20})_2O_{3+\delta}$ was slightly lower than that of $(Yb_{0.85}Pr_{0.15})_2O_{3+\delta}$, because the impurity of Pr_6O_{11} generated might decrease the active sites.

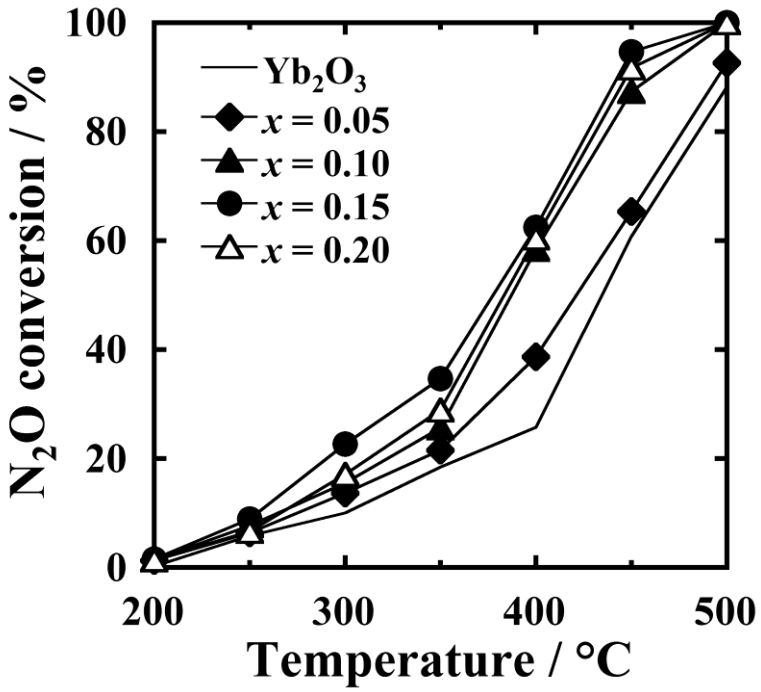

Figure 1-4 Temperature dependencies of the N_2O conversion for $(Yb_{1-x}Pr_x)_2O_{3+\delta}$.

The durability of the $(Yb_{0.85}Pr_{0.15})_2O_{3+\delta}$ catalyst against co-existence gas was investigated. **Figure 1-5** presents the catalytic activity in the presence of water vapor, O_2, or CO_2. The N_2O conversions were almost maintained even in the atmosphere containing high amount of water vapor (3 vol%), O_2 (10 vol%), or CO_2 (10 vol%). In the previous study, the typical spinel-type Co_3O_4 catalyst has been reported to deactivate in the presence of co-existence gas; e.g., the N_2O conversion at 350 °C was decreased from ca. 100 % (without co-existence gas) to ca. 70 % (with 10 % O_2) and ca. 40 % (with 5 % H_2O) [28]. Therefore, it is clear that the $(Yb_{0.85}Pr_{0.15})_2O_{3+\delta}$ catalyst has a high durability against O_2, CO_2, or H_2O.

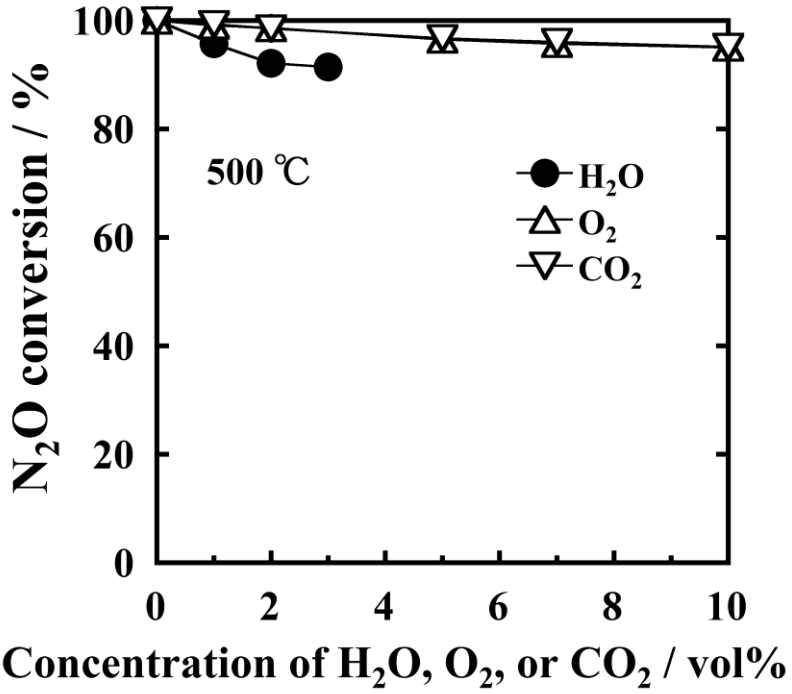

Figure 1-5 Influence of water vapor, O_2, or CO_2 to the N_2O conversion over $(Yb_{0.85}Pr_{0.15})_2O_{3+\delta}$.

1.3.3. Yb_2O_3-Co_3O_4 catalysts

The compositions identified by XRF and the BET surface areas of $(Yb_{1-x}Co_x)_2O_{3-\delta}$ are tabulated in **Table 1-3**. Similar to the case for the $(Yb_{1-x}Pr_x)_2O_{3+\delta}$ catalysts, it was found that the samples contained the expected amounts of cations. The surface area decreased with increasing the Co content, because the Co doping may also induce particle aggregation, as same as the case for $(Yb_{1-x}Pr_x)_2O_{3+\delta}$.

Figure 1-6 shows the XRD patterns of $(Yb_{1-x}Co_x)_2O_{3-\delta}$. The samples with $x \leq 0.10$ have single-phase of cubic C-type structure. For the sample with $x = 0.15$, the impurity phase of Co_3O_4 was observed. The lattice constant is also listed in **Table 1-3**. A lattice shrinkage was observed for the Co-doped samples compared to the Yb_2O_3, and the lattice constant monotonously decreased with increase of Co content (x) up to $x = 0.10$, indicating that the smaller Co ions (Co^{2+}: 0.072 nm, Co^{3+}: 0.063 nm [CN = 6] [27]) were partially substituted the Yb^{3+} (0.101 nm [CN = 6] [27]) sites. For the sample with $x = 0.15$, the lattice constant of the C-type structure maintained almost the same value as the $x = 0.10$ sample. Therefore, it is found that the solid solubility limit composition is $(Yb_{0.90}Co_{0.10})_2O_{3-\delta}$ ($x = 0.10$).

Table 1-3 Composition measured by XRF, BET surface area, and lattice constant of $(Yb_{1-x}Co_x)_2O_{3-\delta}$

Catalyst	Measured composition	Surface area / $m^2 \cdot g^{-1}$	Lattice constant / nm
Yb_2O_3	Yb_2O_3	50.0	1.0461
$(Yb_{0.95}Co_{0.05})_2O_{3-\delta}$	$(Yb_{0.96}Co_{0.04})_2O_{3-\delta}$	39.9	1.0457
$(Yb_{0.90}Co_{0.10})_2O_{3-\delta}$	$(Yb_{0.91}Co_{0.09})_2O_{3-\delta}$	34.8	1.0453
$(Yb_{0.85}Co_{0.15})_2O_{3-\delta}$	$(Yb_{0.85}Co_{0.15})_2O_{3-\delta}$	33.9	1.0452

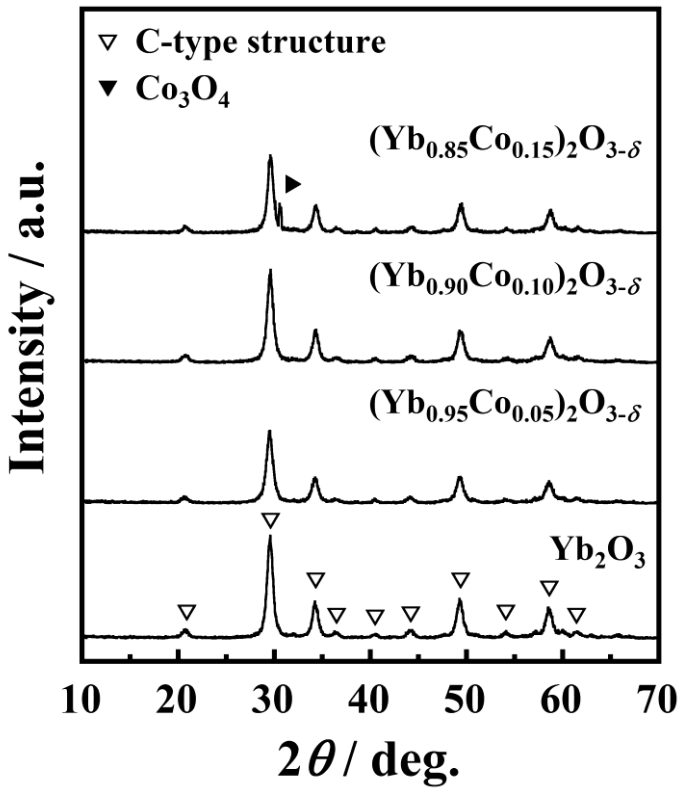

Figure 1-6 XRD patterns of $(Yb_{1-x}Co_x)_2O_{3-\delta}$.

Figure 1-7 shows the temperature dependences of the N_2O decomposition activity for the $(Yb_{1-x}Co_x)_2O_{3-\delta}$ catalysts. With increasing Co content, the catalytic activity was obviously increased in the single-phase region ($x \leq 0.10$), even though the surface areas of the Co-doped samples were lower than that of Yb_2O_3. The enhancement in catalytic activity might be attributed by the improvement of the redox properties due to the valence change of $Co^{2+/3+}$ and by the increase of the N_2O adsorption sites produced by the formation of oxide ion vacancy. Among the single-phase samples ($x \leq 0.10$), the highest activity was obtained for the $(Yb_{0.90}Co_{0.10})_2O_{3-\delta}$ ($x = 0.10$) solid, and N_2O was completely decomposed to N_2 and O_2 at 500 °C, where the formation of neither NO nor

NO_2 were detected. For the $(Yb_{0.85}Co_{0.15})_2O_{3-\delta}$ (x = 0.15) sample, the conversions were lower than the cases for x = 0.10 at each temperature below 500 °C, while N_2O was also completely decomposed at 500 °C, due to the appearance of the impurity phase which might decrease the active sites.

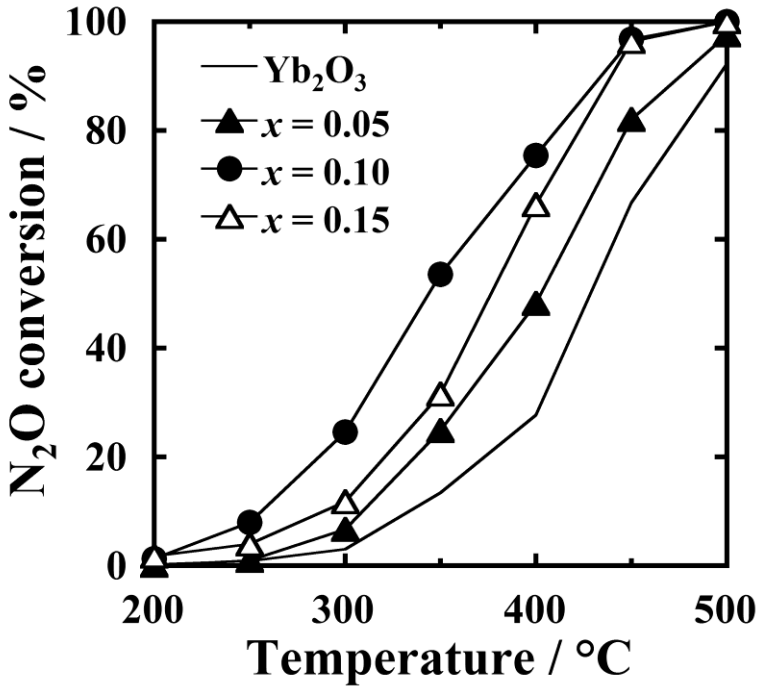

Figure 1-7 Temperature dependencies of the N_2O conversion of the $(Yb_{1-x}Co_x)_2O_{3-\delta}$ catalysts.

In order to confirm the durability of the $(Yb_{0.90}Co_{0.10})_2O_{3-\delta}$ catalyst against co-existing gases, the catalytic activity was evaluated in the presence of water vapor, O_2, or CO_2, and the results are shown in **Figure 1-8**. Since the obvious deterioration in activity was not observed even in the atmosphere containing high amount of water vapor (3 vol%), O_2 gas (10 vol%), and CO_2 gas (10 vol%), the $(Yb_{0.90}Co_{0.10})_2O_{3-\delta}$ catalyst also exhibited a high durability against O_2, CO_2, or H_2O.

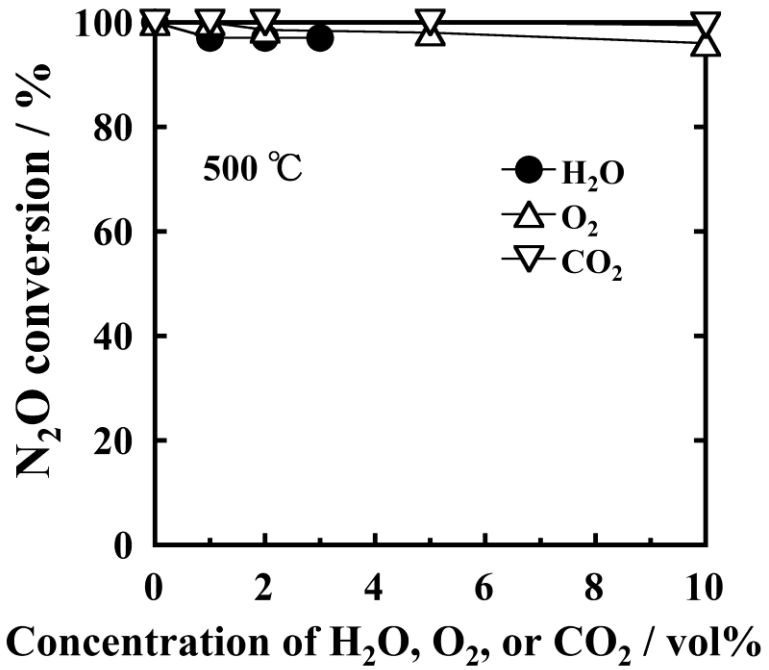

Figure 1-8 Effect of the presence of O_2, CO_2, or H_2O on the N_2O conversion for $(Yb_{0.90}Co_{0.10})_2O_{3-\delta}$.

Figure 1-9 compares the temperature dependencies of the N_2O decomposition activity for the $(Yb_{0.90}Co_{0.10})_2O_{3-\delta}$, the $(Yb_{0.85}Pr_{0.15})_2O_{3+\delta}$, and the Yb_2O_3 solids. Introduction of $Pr^{3+/4+}$ or $Co^{2+/3+}$ improved the catalytic activity compared to Yb_2O_3, indicating that the redox property contributed to the N_2O decomposition. Furthermore, the activity of $(Yb_{0.90}Co_{0.10})_2O_{3-\delta}$ was higher than that of $(Yb_{0.85}Pr_{0.15})_2O_{3+\delta}$ at temperatures between 300 and 450 °C; therefore, the activity was also improved by the formation of oxide ion vacancies.

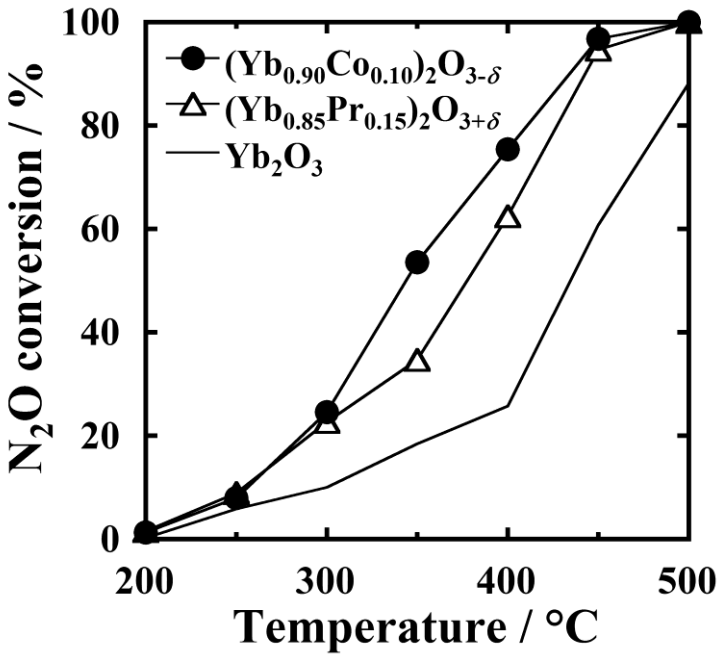

Figure 1-9 Temperature dependencies of the N_2O decomposition for $(Yb_{0.90}Co_{0.10})_2O_{3-\delta}$, $(Yb_{0.85}Pr_{0.15})_2O_{3+\delta}$, and Yb_2O_3.

1.4. Conclusions

In this chapter, novel N_2O decomposition catalysts having high catalytic activities and durabilities for co-existence gases by selecting the cubic C-type R_2O_3 (R = Y, Eu, Gd, Dy, Ho, Er, Tm, Yb, and Lu) as the mother solid are described. Since Yb_2O_3 showed the highest catalytic activity among the C-type R_2O_3 (R = Y, Eu, Gd, Dy, Ho, Er, Tm, Yb, and Lu) solids, Pr_6O_{11} or Co_3O_4 was introduced into the Yb_2O_3 lattice to give the redox property and/or oxide ion vacancy. As a result, the catalytic activity was enhanced by introducing Pr_6O_{11} or Co_3O_4 into the Yb_2O_3 lattice and the highest catalytic activities were obtained for the $(Yb_{0.90}Co_{0.10})_2O_{3-\delta}$ and $(Yb_{0.85}Pr_{0.15})_2O_{3+\delta}$ catalysts for each system, which can decompose N_2O into nitrogen and oxygen gases at temperature as low as 500 °C without influence of the presence of O_2, CO_2, or H_2O. The $(Yb_{0.90}Co_{0.10})_2O_{3-\delta}$ catalyst showed the higher activity than the $(Yb_{0.85}Pr_{0.15})_2O_{3+\delta}$ case probably due to the additional support of oxide ion vacancy in the solid.

Chapter 2

Effect of Oxide Ion Vacancy in the C-type Structure on Direct N_2O Decomposition Activity

2.1. Introduction

In chapter 1, it was described that the Yb_2O_3-Pr_6O_{11} and the Yb_2O_3-Co_3O_4 solids with a cubic C-type structure showed superior N_2O decomposition activities. The C-type structure is related to the fluorite-type structure with removed one-quarter of the oxide ions, hence the oxide ion vacancy in the C-type structure is considered to work as an active site for N_2O decomposition.

As a next study described in this chapter, I investigated the effect of the oxide ion vacancy in the cubic C-type structure on the catalytic activity. Here, I selected ZrO_2-Y_2O_3 solid solution which is known to have fluorite-type or C-type structures depending on their composition. In the compositional region where Y_2O_3 content is small, the solid holds a fluorite-type structure, in which oxide ion vacancies are disordered. For the solids containing large amount of Y_2O_3, the structure transforms to the C-type structure [29]. Furthermore, only the effect of oxide ion vacancy on the N_2O decomposition can be discussed for the ZrO_2-Y_2O_3 solid solutions due to the single valence states of constituent cations (Zr^{4+} and Y^{3+}), meaning that no generation of redox property caused by the valence change of cations. Based on these concepts, I prepared the $Zr_{1-x}Y_xO_{2-\delta}$ solids and investigated their direct N_2O decomposition activities.

2.2. Experimental Procedure

The $Zr_{1-x}Y_xO_{2-\delta}$ solid solutions were synthesized via a co-precipitation method. Stoichiometric amounts of aqueous solutions of 1.0 mol·L^{-1} $Y(NO_3)_3$ and 0.1 mol·L^{-1} $ZrO(NO_3)_2$ were mixed, and mixed solution was added into a 1 mol·L^{-1} ammonium carbonate aqueous solution with stirring at room temperature. With the pH of the solution was adjusted to 9 by dropwise addition of 4 mol·L^{-1} ammonia aqueous solution, the mixture was stirred for 6 h at room temperature. The precipitation product was recovered by suction filtration, dried, and then calcined at 1600 °C for 6 h in atmospheric air.

The composition of the catalyst was confirmed by X-ray fluorescence spectrometry (XRF; Supermini200, Rigaku). The Brunauer-Emmett-Teller (BET) surface area was measured at −196 °C (TriStar 3000, Micromeritics) using nitrogen gas adsorption. The crystal structure was identified by X-ray powder diffraction (XRD; SmartLab, Rigaku) using Cu-Kα radiation (40 kV and 30 mA). The lattice constants were estimated by refining the XRD peak angles using α-alumina as an internal standard.

The catalytic tests for the N_2O direct decomposition were performed using a conventional fixed-bed flow reactor with a 10 mm diameter quartz glass tube (**Figure 1-1 in chapter 1**). Catalytic activities were measured in the temperature range from 400 to 950 °C using thermal conductivity detection type gas chromatography (GC-8AIT, Shimadzu). A gas mixture of 0.5 vol% nitrous oxide-99.5 vol% helium was fed at a rate of 60 mL·min^{-1} over 0.2 g of catalyst, that is a catalyst weight/gas flow rate (W/F) ratio of 0.2 g·s·mL^{-1}. Before the catalytic activity tests, each catalyst was preheated at 200 °C for 1 h in a helium flow.

Diffusion reflectance infrared Fourier transform spectroscopy (DRIFTS) analysis was performed with an *in situ* FT-IR spectrometer (FT/IR-6100, JASCO) under a 0.5 vol% N_2O-99.5 vol% He flow (60 mL·min^{-1}). An environmental DRIFTS chamber was equipped with calcium fluoride windows,

allowing thermal and water resistance. Each spectrum was recorded by averaging 100 scans with a resolution of 4 cm^{-1}, where the spectrum was compensated by that under flowing helium. The measurement for KBr was carried out as a standard. Prior to the measurements, the sample was preheated at 400 °C under a He flow.

2.3. Results and Discussion

Table 2-1 tabulates the compositions of $Zr_{1-x}Y_xO_{2-\delta}$ confirmed by XRF, and the amount of oxide ion vacancy (δ) simply estimated from x value; that is $\delta = x/2$. Here, $YO_{1.5}$ (Y_2O_3) is regarded as the distorted fluorite-related structure with a large amount of oxide ion vacancy ($\delta = 0.5$). The measured compositions of the catalysts were consistent with their stoichiometric values within experimental errors. **Table 2-1** also displays the BET surface area of the catalysts. The surface area decreased with increasing the Y content (x), due to the lower melting point of $YO_{1.5}$ (ca. 2200 °C [30]) compared to that of ZrO_2 (ca. 2700 °C [31]). **Figure 2-1** presents the XRD patterns for the $Zr_{1-x}Y_xO_{2-\delta}$ (x = 0.05, 0.10, 0.20, 0.30, 0.50, 0.70, 0.80, 0.90, 0.95, 1). The samples with x = 0.05, 0.10, 0.20 had a single-phase of cubic fluorite-type structure of ZrO_2 (space group: $Fm\bar{3}m$). In the case of the large number of x (x = 0.80, 0.90, 0.95, 1), the patterns were assigned as the cubic C-type structure of $YO_{1.5}$ (space group: $Ia\bar{3}$). In contrast, the samples with x = 0.30, 0.50, 0.70 were obtained as a mixture of C-type structure and monoclinic ZrO_2 phase. The crystal phase and the lattice constant are also summarized in **Table 2-1**. The lattice constant of the samples with the fluorite-type structure was increased with increasing x, because the Zr^{4+} ion sites (0.098 nm [CN = 8] [27]) were partially replaced by the larger Y^{3+} ions (0.116 nm [CN = 8] [27]). For the C-type solids, the lattice constant also increased with x, indicating the replacement of the Zr^{4+} sites (0.086 nm [CN = 6]) with Y^{3+} (0.104 nm [CN = 6]).

Table 2-1 Measured composition, amount of oxygen vacancy (δ), BET surface area, crystal structure, and lattice constant for the $Zr_{1-x}Y_xO_{2-\delta}$ catalysts

Catalyst	Measured composition	δ	BET surface area / $m^2 \cdot g^{-1}$	Crystal structure	Lattice constant / nm
$YO_{1.5}$	—	0.5	1.24	C-type	1.0616
$Zr_{0.05}Y_{0.95}O_{2-\delta}$	$Zr_{0.04}Y_{0.96}O_{2-\delta}$	0.480	2.55	C-type	1.0612
$Zr_{0.10}Y_{0.90}O_{2-\delta}$	$Zr_{0.10}Y_{0.90}O_{2-\delta}$	0.450	2.92	C-type	1.0607
$Zr_{0.20}Y_{0.80}O_{2-\delta}$	$Zr_{0.20}Y_{0.80}O_{2-\delta}$	0.400	3.48	C-type	1.0600
$Zr_{0.30}Y_{0.70}O_{2-\delta}$	$Zr_{0.31}Y_{0.69}O_{2-\delta}$	0.345	3.56	C-type + Monoclinic	—
$Zr_{0.50}Y_{0.50}O_{2-\delta}$	$Zr_{0.50}Y_{0.50}O_{2-\delta}$	0.250	3.88	C-type + Monoclinic	—
$Zr_{0.70}Y_{0.30}O_{2-\delta}$	$Zr_{0.70}Y_{0.30}O_{2-\delta}$	0.150	3.93	C-type + Monoclinic	—
$Zr_{0.80}Y_{0.20}O_{2-\delta}$	$Zr_{0.81}Y_{0.19}O_{2-\delta}$	0.095	6.20	Fluorite-type	0.5144
$Zr_{0.90}Y_{0.10}O_{2-\delta}$	$Zr_{0.89}Y_{0.11}O_{2-\delta}$	0.055	7.70	Fluorite-type	0.5121
$Zr_{0.95}Y_{0.05}O_{2-\delta}$	$Zr_{0.95}Y_{0.05}O_{2-\delta}$	0.025	8.10	Fluorite-type	0.5103

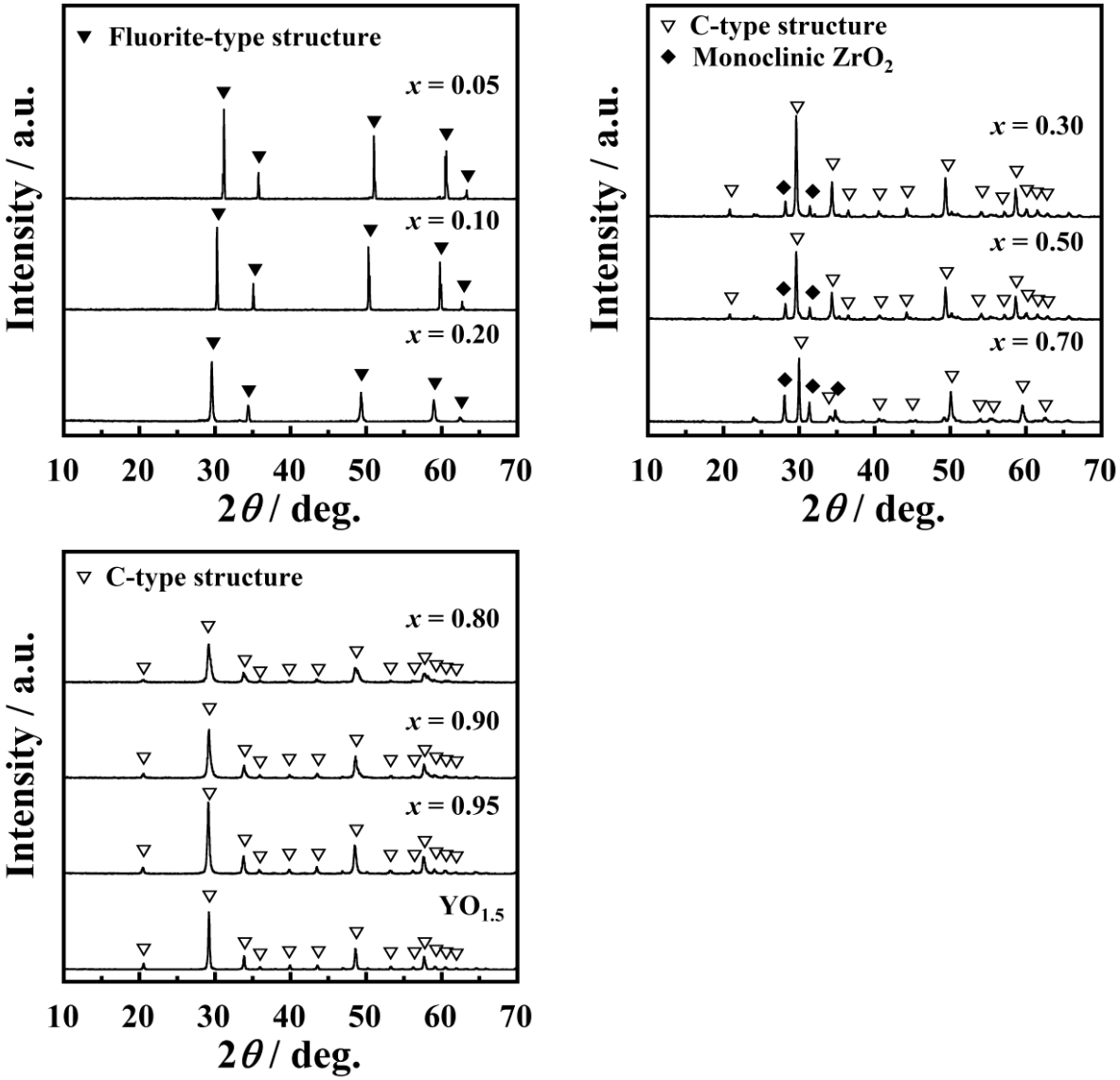

Figure 2-1 XRD patterns of the $Zr_{1-x}Y_xO_{2-\delta}$ (x = 0.05, 0.10, 0.20, 0.30, 0.50, 0.70, 0.80, 0.90, 0.95, 1) solids.

To investigate the effect of oxide ion vacancy to the N_2O decomposition process for the $Zr_{1-x}Y_xO_{2-\delta}$ catalysts, *in situ* FT-IR measurement was carried out under a 0.5 vol% N_2O-99.5 vol% He flow at 50 °C. **Figure 2-2a** shows the DRIFTS spectra of the $Zr_{1-x}Y_xO_{2-\delta}$ catalysts with the data of a standard sample (KBr). In the wavenumber between 3000 and 1000 cm^{-1}, only doublet peaks were observed at ca. 2240 and 2210 cm^{-1}, which were assigned to the asymmetric N-N stretching vibration of N_2O [32, 33]. The N_2O peak intensities of $Zr_{1-x}Y_xO_{2-\delta}$ were higher than those of the standard sample and increased with x, indicating that N_2O was adsorbed on the catalyst surface. The amount of the N_2O adsorption on the surface of solids was estimated from the N_2O peak area by compensating with the corresponding data of the standard sample (KBr). **Figure 2-2b** presents the compensated N_2O adsorption peak area as a function of the amount of oxide ion vacancy (δ). Both the solids having the fluorite-type structure ($0.05 \leq x \leq 0.20$) and the C-type ($x \geq 0.80$) structure, the N_2O adsorption peak area was linearly increased with the increase of oxide ion vacancies (δ). Also, the N_2O adsorption peak areas of the C-type solids were larger than those of the fluorite-type solids, owing to the high δ values in the C-type structure ($\delta \geq 0.4$) compared to the fluorite-type case ($\delta \leq 0.1$). These results indicate that the oxide ion vacancies work as the N_2O adsorption sites on the catalyst surface and the C-type structure can hold a large amount of oxide ion vacancy stably in its lattice.

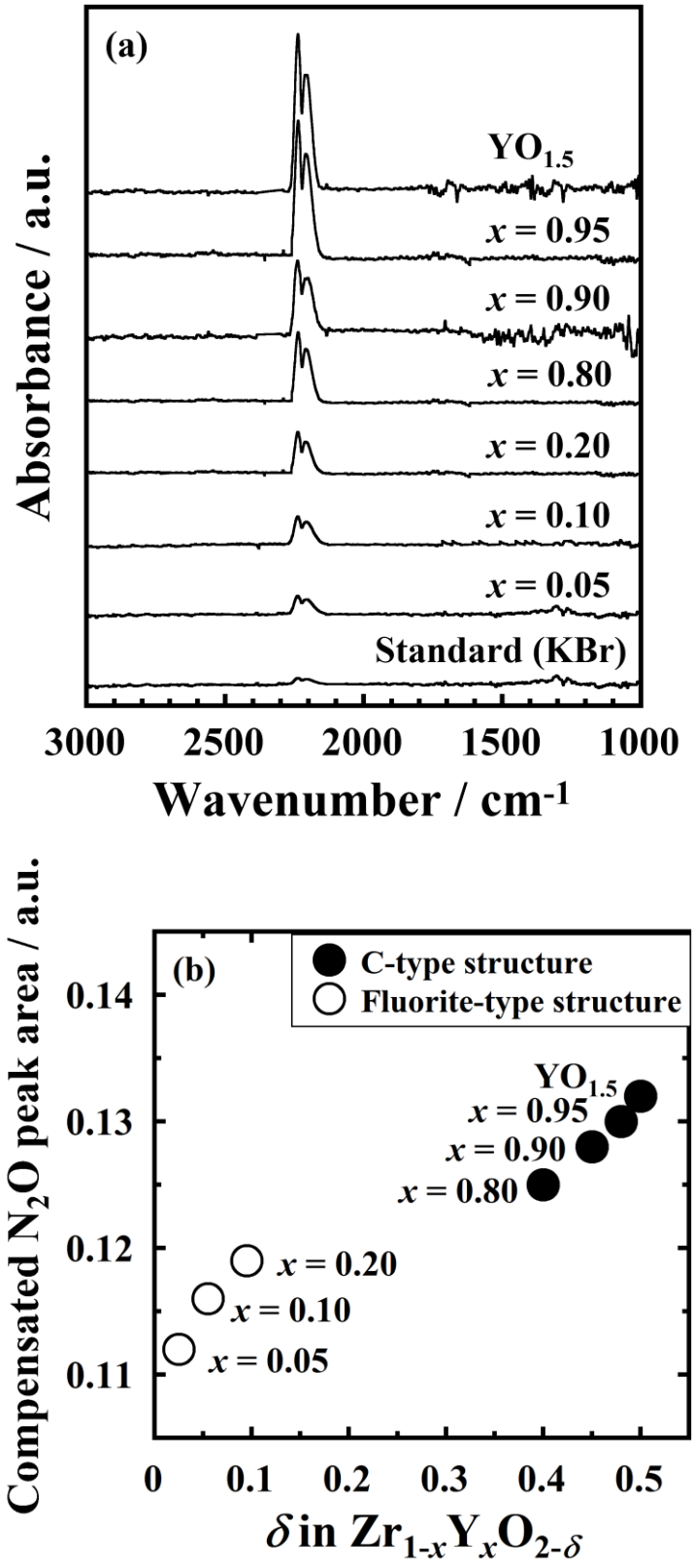

Figure 2-2 (a) DRIFTS spectra of $Zr_{1-x}Y_xO_{2-\delta}$ and (b) relationship between oxide ion vacancies and the compensated N_2O peak area.

Figure 2-3 shows the temperature dependence of the N_2O conversion for the $Zr_{1-x}Y_xO_{2-\delta}$ catalysts with a single phase of fluorite-type and C-type structures. The catalytic activity continuously increased with increasing x, and the highest activity was obtained for the $YO_{1.5}$ ($x = 1$) solid with C-type structure while the surface area decreased.

To discuss deeply effect of oxide ion vacancy to the catalytic activity, the apparent activation energy for the N_2O decomposition was calculated using **equations 2-1 and 2-2**.

$$r = k\,C \qquad (2\text{-}1)$$

$$k = A\exp(-E_a / RT) \qquad (2\text{-}2)$$

, where r is the reaction rate, k is the apparent rate constant, C is the N_2O concentration, A is the pre-exponential factor, E_a is the apparent activation energy, R is the gas constant, and T is the reaction temperature. The apparent activation energy for the N_2O decomposition can be obtained from the slope of the Arrhenius plot, in which ln k is plotted against the reciprocal temperature. **Figure 2-4** depicts the relationship between the apparent activation energy and the amount of oxide ion vacancy. The apparent activation energy lowered with increasing the amount of oxide ion vacancy for each series. In addition, the catalysts with C-type structure exhibited the lower apparent activation energy compared with the fluorite-type solids, because the C-type solids hold higher amount of oxide ion vacancy than the fluorite-type case. From these results, it was found that the oxide ion vacancies effectively worked as the N_2O adsorption sites and the catalytic active sites, and that the C-type structure having a much amount of oxide ion vacancy stably can facilitate the N_2O decomposition.

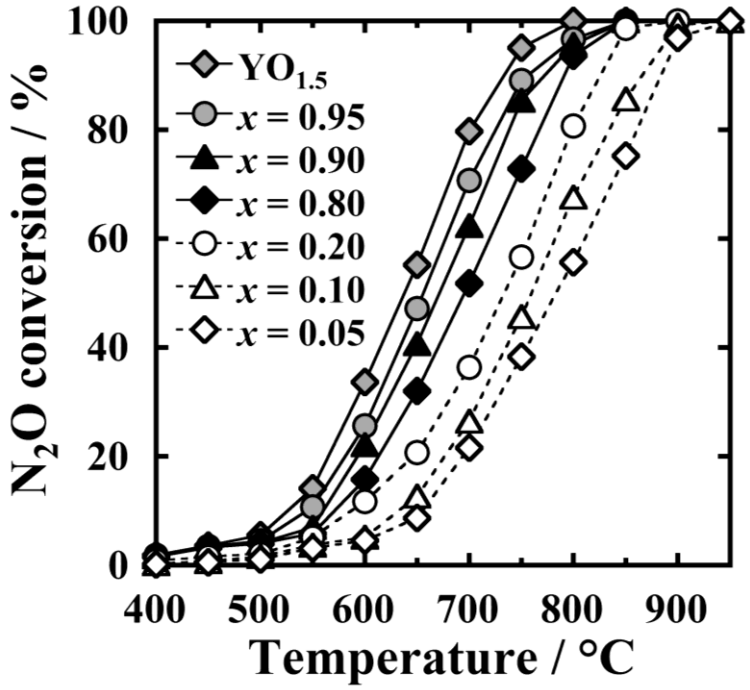

Figure 2-3 Temperature dependence of the N_2O conversion for $Zr_{1-x}Y_xO_{2-\delta}$.

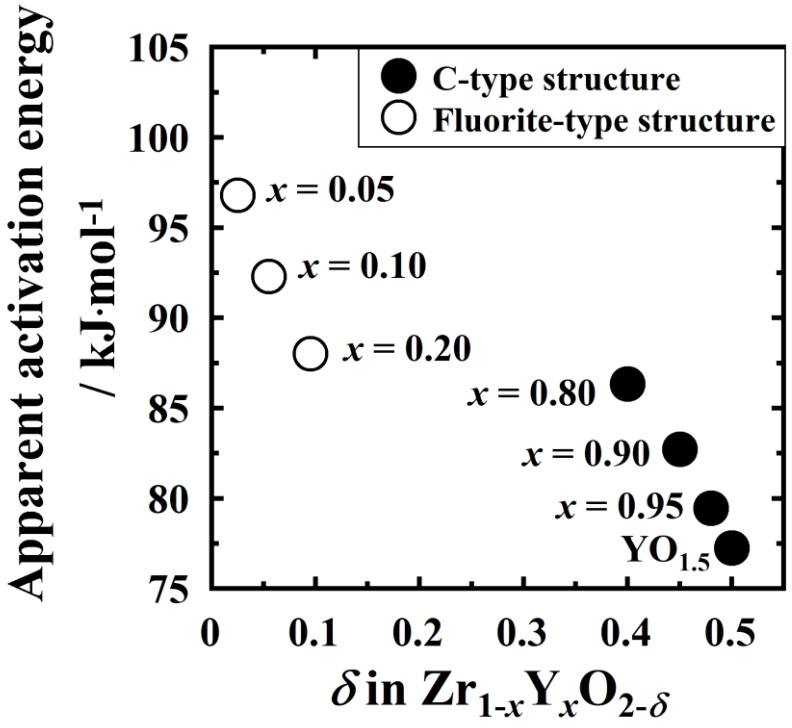

Figure 2-4 Relationship between the apparent activation energy for the N_2O decomposition and the amount of oxide ion vacancy, δ.

2.4. Conclusions

The effect of the oxide ion vacancy in the C-type structure to the N_2O decomposition activity was investigated by selecting the $Zr_{1-x}Y_xO_{2-\delta}$ solid solutions whose crystal structure is changed between the C-type and fluorite-type structures with the composition. Both the solids having C-type and fluorite-type structures showed a general tendency that the amount of the N_2O adsorption and the catalytic activity were improved with increasing the oxide ion vacancies (δ) in $Zr_{1-x}Y_xO_{2-\delta}$. Furthermore, it was clear that the solids with C-type structure exhibited higher activity than the fluorite-type solids due to the existence of large amount of oxide ion vacancy. By the systematic investigation of the catalytic activity with changing the amount of oxide ion vacancy in the crystal structure, it is demonstrated that the C-type structure which can contain large amount of oxide ion vacancy in its structure is suitable for the N_2O decomposition.

Chapter 3

Effects of Redox Property and Oxide Ion Vacancy on Direct N_2O Decomposition Activity

3.1. Introduction

As mentioned in chapter 1, the doping of $Pr^{3+/4+}$ or $Co^{2+/3+}$ ions into the cubic C-type Yb_2O_3 lattice improved the catalytic activity likely due to the redox behavior of $Pr^{3+/4+}$ or $Co^{2+/3+}$. For the Co-doped catalysts, the formation of oxide ion vacancy is considered to be another reason for the enhancement in activity.

In this chapter, the effects of the redox property and the oxide ion vacancy on the catalytic activity are described. To this end, I additionally selected the $Cu^{+/2+}$, Sr^{2+}, and Zr^{4+} ions as a dopant in addition to $Pr^{3+/4+}$ and $Co^{2+/3+}$. Here, Cu can hold a monovalent state of Cu^{+}, which is lower valence state than the Co^{2+} case, suggesting that generation of much amount of oxide ion vacancies was expected. Moreover, electronic conduction caused by the valence change of $Cu^{+/2+}$ should occur smoothly, similar to the case for $Pr^{3+/4+}$ and $Co^{2+/3+}$, which may affect the N_2O decomposition. The cations, Sr^{2+} and Zr^{4+}, were chosen as those holding only divalent and tetravalent states stably, respectively, because these cations can generate the oxide ion vacancies without appearance of redox behavior by the substitution. Thus, the N_2O decomposition activities of the Yb_2O_3-MO_x (M = Pr, Co, Cu, Sr, Zr) solid solutions were compared to discuss the effects of the redox properties and the oxide ion vacancy on the catalytic activity.

3.2. Experimental Procedure

The $(Yb_{0.90}M_{0.10})_2O_{3-\delta}$ (M = Pr, Co, Cu, Sr, Zr) catalysts were synthesized via a co-precipitation method. A stoichiometric mixtures of 1 mol·L^{-1} $Yb(NO_3)_3$ and 1 mol·L^{-1} metal nitrate of ($Pr(NO_3)_3$, $Co(NO_3)_2$, $Cu(NO_3)_2$, $Sr(NO_3)_2$, or $ZrO(NO_3)_2$) aqueous solutions were added into a 1 mol·L^{-1} $(NH_4)_2CO_3$ aqueous solution and stirred vigorously. The pH value of the mixture was kept at 9 by dropwise addition of 4 mol·L^{-1} ammonia aqueous solution, and further stirred for 6 h at room temperature. The precipitation product was recovered by suction filtration, dried, and then calcined at 500 °C for 6 h in the air.

The composition of the catalyst was investigated by X-ray fluorescence spectrometry (XRF; Supermini200, Rigaku). The Brunauer-Emmett-Teller (BET) surface area was measured at −196 °C (TriStar 3000, Micromeritics) using nitrogen gas adsorption. The crystal structure was identified by X-ray powder diffraction (XRD; MultiFlex, Rigaku) using Cu-Kα radiation (40 kV and 40 mA). Structural parameters were determined by Rietveld refinement with a RIETAN-FP program [34]. X-ray photoelectron spectroscopy (XPS; PHI 5000 VersaProbe II, ULVAC-PHI, or Axis Ultra DLD, Kratos) was performed at room temperature using Al-Kα radiation. The influence of charging on the binding energies was corrected with respect to the C 1s peak at 284.6 eV, and the spectra were fit using a Shirley background and Gaussian-Lorentzian line shapes.

H_2 temperature programmed reduction (H_2-TPR) experiments were carried out under a 50 mL·min^{-1} flow of 5 vol% H_2-95 vol% Ar at a heating rate of 10 °C·min^{-1} (Belcat-B, MicrotracBEL). Diffusion reflectance infrared transform spectroscopy (DRIFTS) analysis was performed with an *in situ* FTIR spectrophotometer (FT/IR-6100, JASCO) under 0.5 vol% N_2O-99.5 vol% He flow (60 mL·min^{-1}). An environmental DRIFTS chamber was equipped with CaF_2 windows, allowing thermal and water resistance. All spectra were recorded after averaging 100 scans with a resolution of 4 cm^{-1}.

Before the measurements, the sample was heated under He flow at 400 °C. In addition, a KBr solid was also measured as a standard sample. Each spectrum was compensated by that under flowing He.

3.3. Results and Discussion

The compositions measured by XRF and the BET surface areas of $(Yb_{0.90}M_{0.10})_2O_{3-\delta}$ (M = Pr, Co, Cu, Sr, Zr) and Yb_2O_3 are summarized in **Table 3-1**. The measured compositions were confirmed to be in good agreement with their feed values within experimental errors. The surfaces area of $(Yb_{0.90}M_{0.10})_2O_{3-\delta}$ were lower than that of Yb_2O_3, because the introduction of dopant ions might induce particle aggregation.

Table 3-1 Measured composition and BET surface area of $(Yb_{0.90}M_{0.10})_2O_{3-\delta}$ (M = Pr, Co, Cu, Sr, Zr)

Catalyst	Measured composition	BET surface area / $m^2 \cdot g^{-1}$
$(Yb_{0.90}Zr_{0.10})_2O_{3-\delta}$	$(Yb_{0.90}Zr_{0.10})_2O_{3-\delta}$	48.0
$(Yb_{0.90}Sr_{0.10})_2O_{3-\delta}$	$(Yb_{0.90}Sr_{0.10})_2O_{3-\delta}$	40.1
$(Yb_{0.90}Cu_{0.10})_2O_{3-\delta}$	$(Yb_{0.90}Cu_{0.10})_2O_{3-\delta}$	35.4
$(Yb_{0.90}Co_{0.10})_2O_{3-\delta}$	$(Yb_{0.90}Co_{0.09})_2O_{3-\delta}$	31.5
$(Yb_{0.90}Pr_{0.10})_2O_{3-\delta}$	$(Yb_{0.90}Pr_{0.10})_2O_{3-\delta}$	39.9
Yb_2O_3	—	50.4

Figure 3-1 shows the results of the Rietveld refinement of the XRD patterns for the $(Yb_{0.90}M_{0.10})_2O_{3-\delta}$ (M = Pr, Co, Cu, Sr, Zr) catalysts, where the cationic ratios of Yb and M were fixed as those obtained from the XRF results. The structural parameters are listed in **Table 3-2**. For the M = Pr and Zr samples, a satisfactory fitting was obtained when the additional oxide ions located

at 16*c* site. All catalysts had single-phase of the cubic C-type structure (space group: $Ia\bar{3}$). The lattice constants of the M = Pr, Sr samples were larger than that of Yb_2O_3, because the larger Pr or Sr ions (Pr^{3+}: 0.113 nm, Sr^{2+}: 0.131 nm [CN = 6] [27]) were partially occupied the Yb^{3+} (0.101 nm [CN = 6] [27]) sites. In contrast, the lattice shrinkage was observed for the M = Co, Cu, Zr samples, due to the replacement of the Yb^{3+} (0.101 nm [CN = 6]) sites by the smaller Cu, Co, or Zr ions (Cu^{+}: 0.091 nm, Cu^{2+}: 0.087, Co^{3+}: 0.068 nm, Co^{2+}: 0.072 nm, Zr^{4+}: 0.086 nm [CN = 6] [27]). As tabulated in **Table 3-2**, the oxygen occupation at 48*e* site of $(Yb_{0.90}M_{0.10})_2O_{3-\delta}$ (M = Co, Cu, Sr) were less than unity, indicating that oxide ion vacancies were successfully formed. Amounts of oxygen vacancy (δ) of $(Yb_{0.90}M_{0.10})_2O_{3-\delta}$ (M = Co, Cu, Sr) were estimated to be 0.082, 0.107, and 0.090. For the M = Pr and Zr samples, the excess amount of oxygen should be introduced by doping a tetravalent Pr^{4+} or Zr^{4+} into the Yb^{3+} site. As a result, the additional oxide ion site was generated at 16*c* site with low occupancy. Since the oxygen occupancy at 48*e* site was fixed to be 1, the δ values of $(Yb_{0.90}M_{0.10})_2O_{3-\delta}$ (M = Pr, Zr) were calculated to be −0.088 and −0.111, respectively.

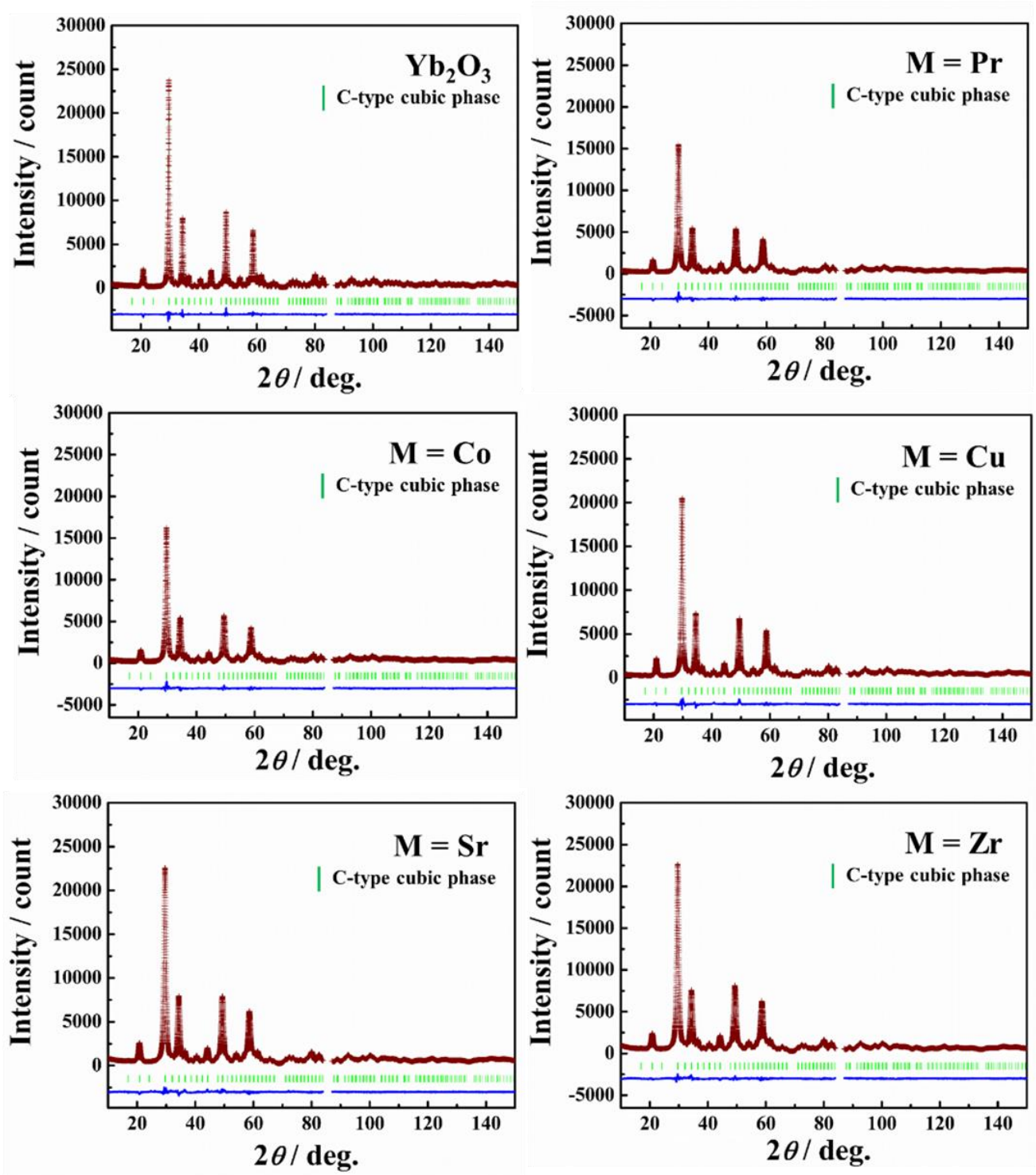

Figure 3-1 Results of Rietveld analysis for $(Yb_{0.90}M_{0.10})_2O_{3-\delta}$ (M = Pr, Co, Cu, Sr, Zr) and Yb_2O_3.

Table 3-2 Structural parameters of C-type structure determined by the Rietveld refinement for the Yb_2O_3 and the $(Yb_{0.90}M_{0.10})_2O_{3-\delta}$ (M = Pr, Co, Cu, Sr, Zr) solids

Sample	Atom	Wyckoff position	Occupancy	*x*	*y*	*z*	*B* / Å
Yb_2O_3	Yb1	8*b*	1	1/4	1/4	1/4	0.5
	Yb2	24*d*	1	−0.032(1)	0	1/4	0.5
	O1	48*e*	1	0.393(1)	0.152(2)	0.380(1)	0.5
	Space group: $Ia\bar{3}$, a = 1.0461(1) nm, R_{wp} = 5.23 %, S = 1.32						
M = Pr	Yb1	8*b*	0.90	1/4	1/4	1/4	0.5
	Pr1	8*b*	0.10	1/4	1/4	1/4	0.5
	Yb2	24*d*	0.90	−0.029(1)	0	1/4	0.5
	Pr2	24*d*	0.10	= *x*(Yb2)	0	1/4	0.5
	O1	48*e*	1	0.389(1)	0.153(1)	0.379(1)	0.5
	O2	16*c*	0.030(1)	0.096(1)	= *x*(O2)	= *x*(O2)	0.5
	Space group: $Ia\bar{3}$, a = 1.0465(1) nm, R_{wp} = 6.05 %, S = 1.45						
M = Co	Yb1	8*b*	0.91	1/4	1/4	1/4	0.5
	Co1	8*b*	0.09	1/4	1/4	1/4	0.5
	Yb2	24*d*	0.91	−0.032(1)	0	1/4	0.5
	Co2	24*d*	0.09	= *x*(Yb2)	0	1/4	0.5
	O1	48*e*	0.975(1)	0.390(2)	0.153(1)	0.380(1)	0.5
	Space group: $Ia\bar{3}$, a = 1.0453(2) nm, R_{wp} = 5.81 %, S = 1.36						
M = Cu	Yb1	8*b*	0.90	1/4	1/4	1/4	0.5
	Cu1	8*b*	0.10	1/4	1/4	1/4	0.5
	Yb2	24*d*	0.90	−0.032(1)	0	1/4	0.5
	Cu2	24*d*	0.10	= *x*(Yb2)	0	1/4	0.5
	O1	48*e*	0.964(1)	0.389(1)	0.153(1)	0.379(1)	0.5
	Space group: $Ia\bar{3}$, a = 1.0454(1) nm, R_{wp} = 4.90 %, S = 1.30						
M = Sr	Yb1	8*b*	0.90	1/4	1/4	1/4	0.5
	Sr1	8*b*	0.10	1/4	1/4	1/4	0.5
	Yb2	24*d*	0.90	−0.032(1)	0	1/4	0.5
	Sr2	24*d*	0.10	= *x*(Yb2)	0	1/4	0.5
	O1	48*e*	0.970(1)	0.390(1)	0.153(1)	0.379(1)	0.5
	Space group: $Ia\bar{3}$, a = 1.0475(1) nm, R_{wp} = 4.50%, S = 1.46						
M = Zr	Yb1	8*b*	0.90	1/4	1/4	1/4	0.5
	Zr1	8*b*	0.10	1/4	1/4	1/4	0.5
	Yb2	24*d*	0.90	−0.032(1)	0	1/4	0.5
	Zr2	24*d*	0.10	= *x*(Yb2)	0	1/4	0.5
	O1	48*e*	1	0.391(2)	0.155(1)	0.380(1)	0.5
	O2	16*c*	0.037(1)	0.095(1)	= *x*(O2)	= *x*(O2)	0.5
	Space group: $Ia\bar{3}$, a = 1.0459(1) nm, R_{wp} = 6.05 %, S = 1.45						

The valence states of the dopant cations in the $(Yb_{0.90}M_{0.10})_2O_{3-\delta}$ (M = Pr, Co, Cu, Sr, Zr) samples were investigated by XPS. **Figure 3-2** presents the XPS spectra of (a) Pr 3d, (b) Co 2p, (c) Cu 2p, (d) Sr 3d, and (e) Zr 3d core-levels for $(Yb_{0.90}M_{0.10})_2O_{3-\delta}$ (M = Pr, Co, Cu, Sr, Zr), respectively. The peaks detected for the $(Yb_{0.90}M_{0.10})_2O_{3-\delta}$ (M = Pr, Co, Cu) solids can be attributed to Cu^{+} and Cu^{2+}, Co^{2+} and Co^{3+}, and Pr^{3+} and Pr^{4+}, respectively. From these spectra, cationic ratio in each solid was calculated to be Pr^{3+}:Pr^{4+} = 43:57, Co^{2+}:Co^{3+} = 52:48, and Cu^{+}:Cu^{2+} = 54:46. The XPS peaks of the $(Yb_{0.90}M_{0.10})_2O_{3-\delta}$ (M = Sr and Zr) samples were identified to be divalent Sr^{2+} and tetravalent Zr^{4+}, respectively.

The XPS spectra of Yb 4d core-levels of the $(Yb_{0.90}M_{0.10})_2O_{3-\delta}$ (M = Pr, Co, Cu, Sr, Zr) samples were shown in **Figure 3-3**. All peaks were assigned as the model spectrum of the trivalent Yb^{3+} ions [35].

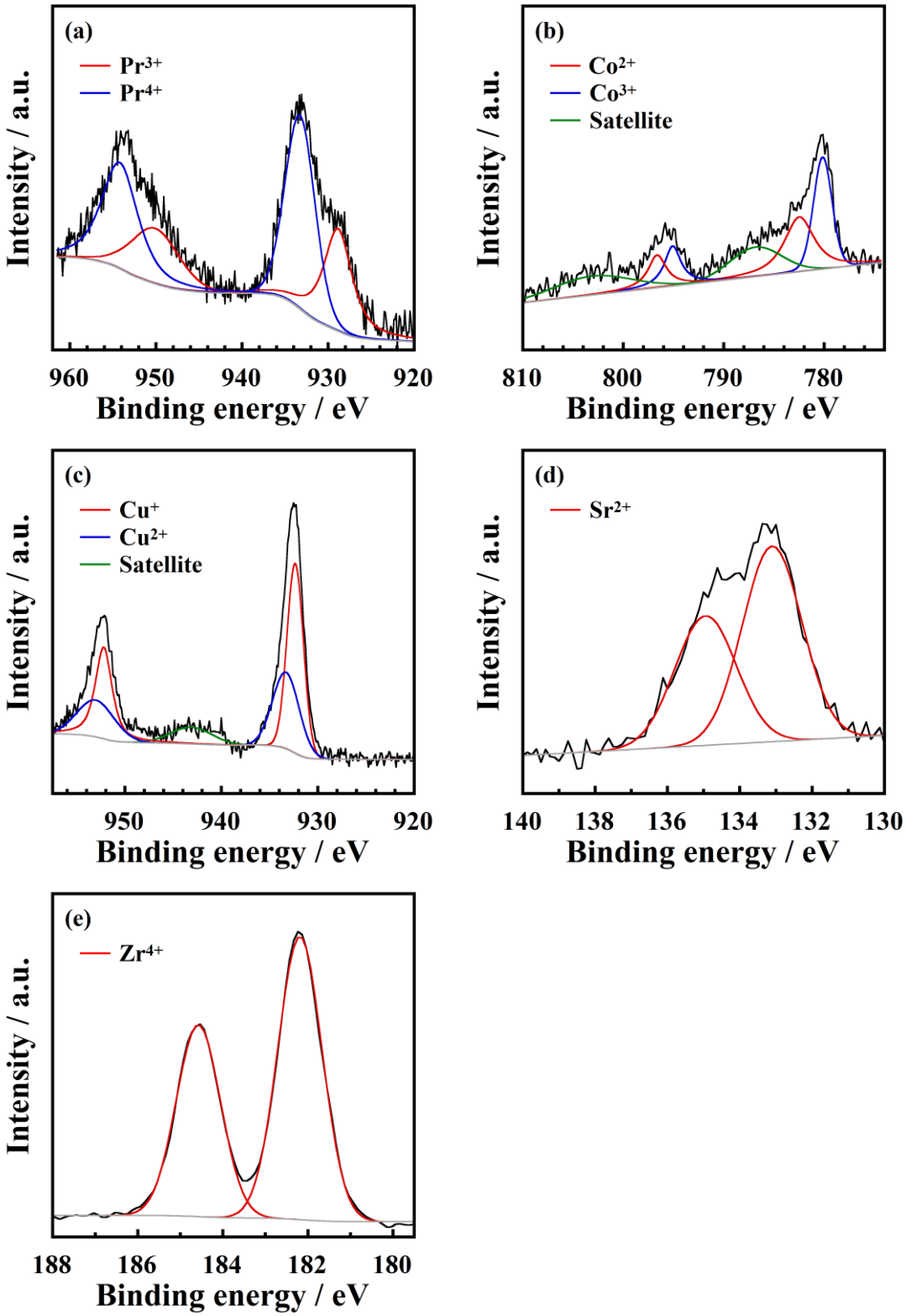

Figure 3-2 XPS spectra of (a) Pr 3d, (b) Co 2p, (c) Cu 2p, (d) Sr 3d, (e) Zr 3d core-levels of $(Yb_{0.90}M_{0.10})_2O_{3-\delta}$.

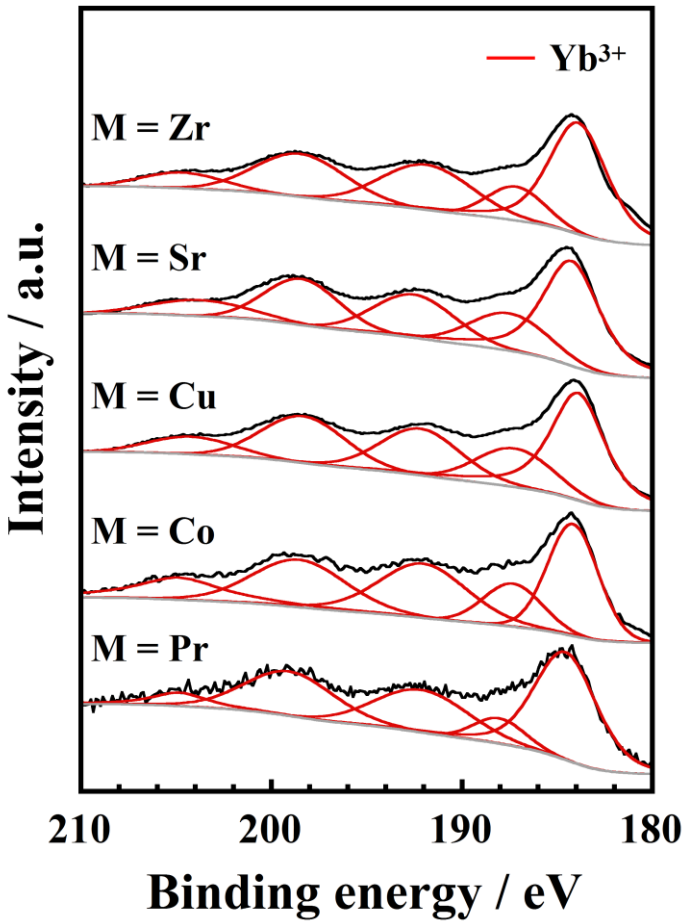

Figure 3-3 XPS spectra of Yb 4d core-levels of the $(Yb_{0.90}M_{0.10})_2O_{3-\delta}$ (M = Pr, Co, Cu, Sr, Zr) catalysts.

To investigate the N_2O adsorption behavior of the $(Yb_{0.90}M_{0.10})_2O_{3-\delta}$ (M = Pr, Co, Cu, Sr, Zr) catalysts, *in situ* FTIR measurements were performed under 0.5%N_2O-99.5%He gas flow at 50 °C. **Figure 3-4a** shows the FTIR spectra with the corresponding data for a standard sample (KBr). In the wavenumber range between 3000 and 1000 cm^{-1}, only doublet peaks were observed at ca. 2240 and 2210 cm^{-1}, corresponding to the asymmetric N-N stretching vibration of N_2O [32, 33]. Since the N_2O peak intensities of the $(Yb_{0.90}M_{0.10})_2O_{3-\delta}$ catalysts were higher than those of the standard sample, it was confirmed that N_2O was adsorbed on the catalyst surface. By introducing the lower valence cations, $Co^{2+/3+}$, $Cu^{+/2+}$, or Sr^{2+}, into the Yb_2O_3 lattice, the intensities of the N_2O peaks were increased compared to those of Yb_2O_3. In contrast, the introduction of higher valence $Pr^{3+/4+}$ or Zr^{4+} caused the lower N_2O peak intensities than those of Yb_2O_3. From the peak area for N_2O, the amount of N_2O adsorption was estimated by compensating the standard sample data. **Figure 3-4b** presents the relationship between the compensated N_2O adsorption peak area and the δ value. The peak area was substantially increased with increasing the δ value, indicating that the N_2O adsorption was influenced by the amount of oxide ion vacancy. Therefore, it was clear that the oxide ion vacancies work as the N_2O adsorption site even for the solids doped various kinds of cations, similar to the result described in chapter 2.

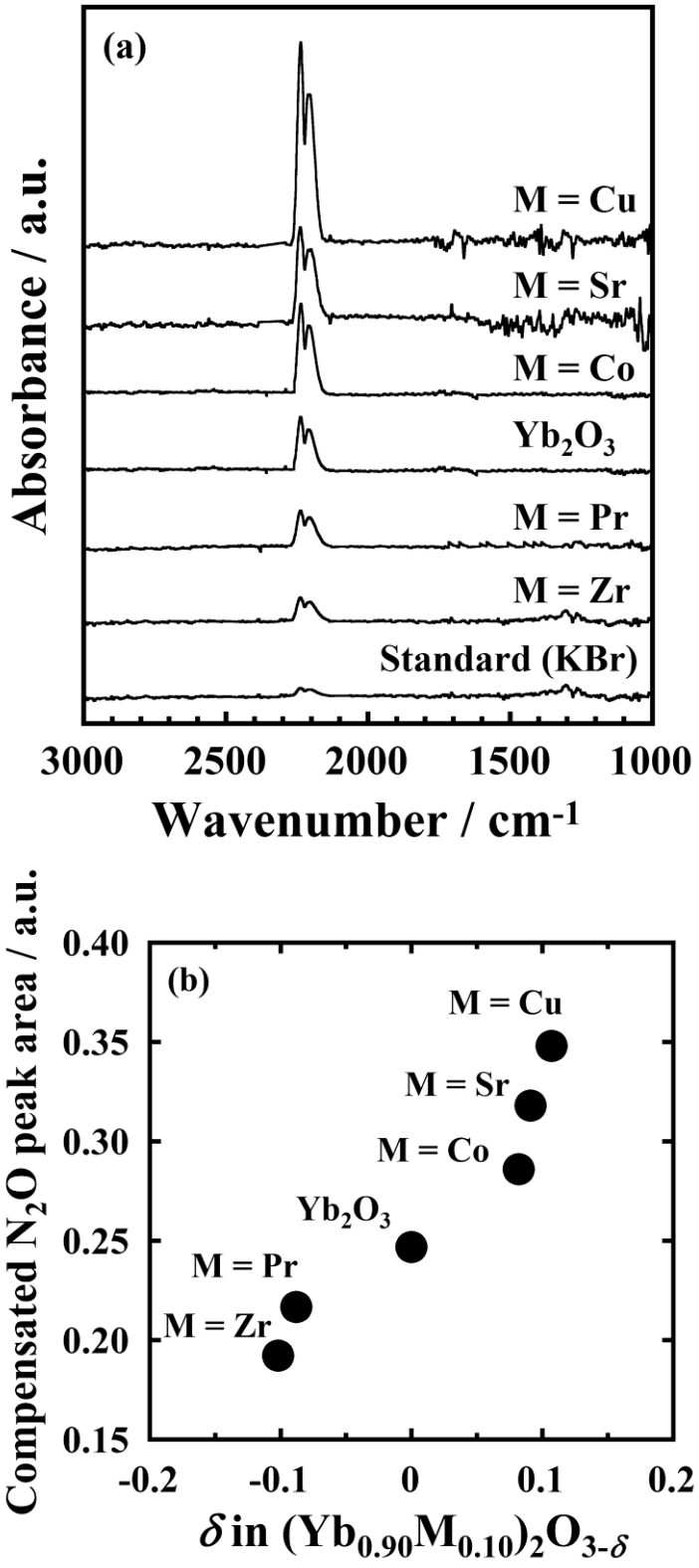

Figure 3-4 DRIFTS spectra of (a) $(Yb_{0.90}M_{0.10})_2O_{3-\delta}$ (M = Pr, Co, Cu, Sr, Zr) under flowing 0.5 vol% N_2O-99.5 vol% He at 50 °C. (b) The change of the compensated N_2O adsorption peak area as a function of the amount of oxide ion vacancy (δ).

H_2-TPR experiments were carried out over $(Yb_{0.90}M_{0.10})_2O_{3-\delta}$ (M = Pr, Co, Cu, Sr, Zr) to investigate their redox properties. TPR profiles of these catalysts are shown in **Figure 3-5**. For the Yb_2O_3 and the M = Sr, Zr samples which may not exhibit redox property caused by the valence change of dopant cations, the reduction peaks were observed only at ca. 450 °C, which can be attributed the reduction from Yb^{3+} to Yb^{2+}. The reduction peaks for the M = Sr, Zr samples were shifted toward high temperature compared to that for Yb_2O_3, indicating that the reducibility was decreased by introducing Sr or Zr ions likely due to the decrease of the Yb^{3+} amount and the lowering of the surface area. For the M = Pr, Co, Cu samples, additional reduction peaks were appeared at 364, 253, and 159 °C, respectively. The peak at 364 °C for $(Yb_{0.90}Pr_{0.10})_2O_{3-\delta}$ is assigned as the reduction of Pr^{4+} to Pr^{3+} [36]. The peak at 253 °C for $(Yb_{0.90}Co_{0.10})_2O_{3-\delta}$ is corresponding to the reduction of Co^{3+} to Co^{2+} [37]. The peak at 159 °C for $(Yb_{0.90}Cu_{0.10})_2O_{3-\delta}$ is by the reduction of Cu^{2+} to Cu^{+} [38]. These results implied the reducibility was enhanced by introducing $Pr^{3+/4+}$, $Co^{2+/3+}$, and $Cu^{+/2+}$ ions. From the first reduction peak temperatures, the order of the redox property was speculated to be $(Yb_{0.90}Cu_{0.10})_2O_{3-\delta}$ > $(Yb_{0.90}Co_{0.10})_2O_{3-\delta}$ > $(Yb_{0.90}Pr_{0.10})_2O_{3-\delta}$ > Yb_2O_3 ≳ $(Yb_{0.90}Sr_{0.10})_2O_{3-\delta}$ ≳ $(Yb_{0.90}Zr_{0.10})_2O_{3-\delta}$.

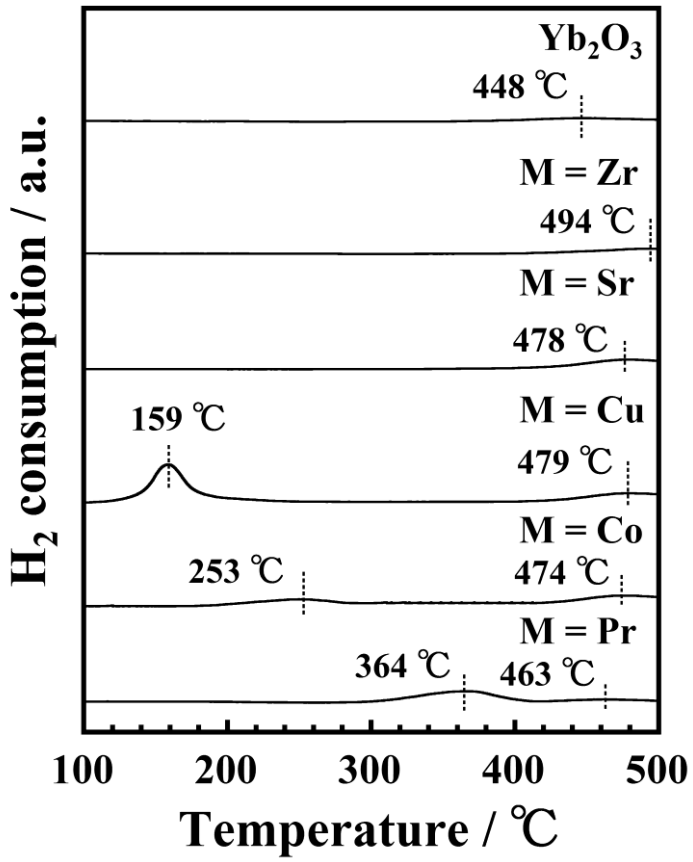

Figure 3-5 H_2-TPR profiles of Yb_2O_3 and $(Yb_{0.90}M_{0.10})_2O_{3-\delta}$ (M = Pr, Co, Cu, Sr, Zr).

The N_2O decomposition activities for the $(Yb_{0.90}M_{0.10})_2O_{3-\delta}$ (M = Pr, Co, Cu, Sr, Zr) catalysts as a function of temperature are shown in **Figure 3-6**. The catalytic activities were obviously enhanced by introducing the Pr, Co, Cu ions into Yb_2O_3 because of the improvement of the redox properties. In particular, the M = Co, Cu catalysts showed the higher activities than that of the M = Pr catalyst, due to a help of the formation of oxide ion vacancy.

For the M = Sr catalyst, the activity was improved compared to that of Yb_2O_3, while the redox property was lower than the Yb_2O_3 case. This result suggests that the formation of oxide ion vacancy also affects the catalytic activity. In contrast, the M = Zr catalyst showed the lowest activity among

the prepared catalysts, because the oxide ion vacancy and the redox property simultaneously decreased. From these results, it is clear that the redox property and the oxide ion vacancy affect the catalytic N_2O decomposition activity.

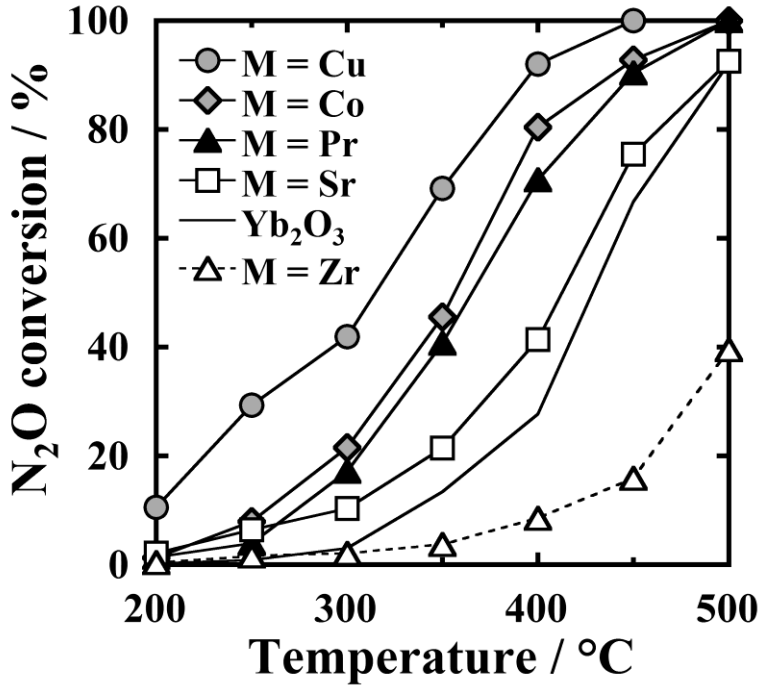

Figure 3-6 Temperature dependencies of the N_2O conversion for the $(Yb_{0.90}M_{0.10})_2O_{3-\delta}$ (M = Pr, Co, Cu, Sr, Zr) catalysts.

For further investigation of the effects of the redox property and the oxide ion vacancy on the catalytic activity, the apparent activation energy for the N_2O decomposition was estimated from the Arrhenius plot using **eqs. 2-1 and 2-2** described in chapter 2.

Figure 3-7a shows the correlation between the apparent activation energy and the reduction temperature in the TPR profile for the $(Yb_{0.90}M_{0.10})_2O_{3-\delta}$ (M = Pr, Co, Cu, Sr, Zr) catalysts. The apparent activation energy lowered substantially with lowering the reduction temperature. Therefore,

the improvement of the redox property is considered to lead the enhancement of the catalytic N_2O decomposition, because the redox behavior may facilitate the removal of adsorbed oxygen species generated in the N_2O decomposition process. Regardless of almost the same redox properties for the Sr and Zr samples, the apparent activation energies were quite different, suggesting that the oxide ion vacancies also affected to the catalytic activity.

Figure 3-7b shows the relation between the apparent activation energy and the amount of oxide ion vacancy (δ). In the region of $\delta \geq 0$, the oxide ion vacancies were formed in the C-type structure. In this compositional range, the apparent activation energies of $(Yb_{0.90}M_{0.10})_2O_{3-\delta}$ (M = Co, Cu, Sr) were lower than that of Yb_2O_3, indicating that the oxide ion vacancies worked as the additional active sites for the N_2O decomposition. In addition, the high redox properties of the M = Co, Cu samples lead to the further lowering of the apparent activation energy, compared to the M = Sr sample. In the region of $\delta < 0$, the apparent activation energy of the M = Zr sample was higher than that of Yb_2O_3, because the N_2O adsorption might be prevented by the excess oxide ions in the lattice, which are located at the additional interstitial oxygen site (16*c*). This result also suggests that the oxide ion vacancies in the C-type structure worked as the active sites. For the M = Pr sample, the apparent activation energy was lowered compared to the Yb_2O_3 case because of its redox property, regardless of the decrease of the amount of oxide ion vacancy.

From these results, it is clear that the catalytic activity for the N_2O decomposition is influenced by both the redox property and the oxide ion vacancy. Also, the highest catalytic activity was obtained for the sample with M = Cu, which possessed the highest redox property and the highest amount of oxide ion vacancy.

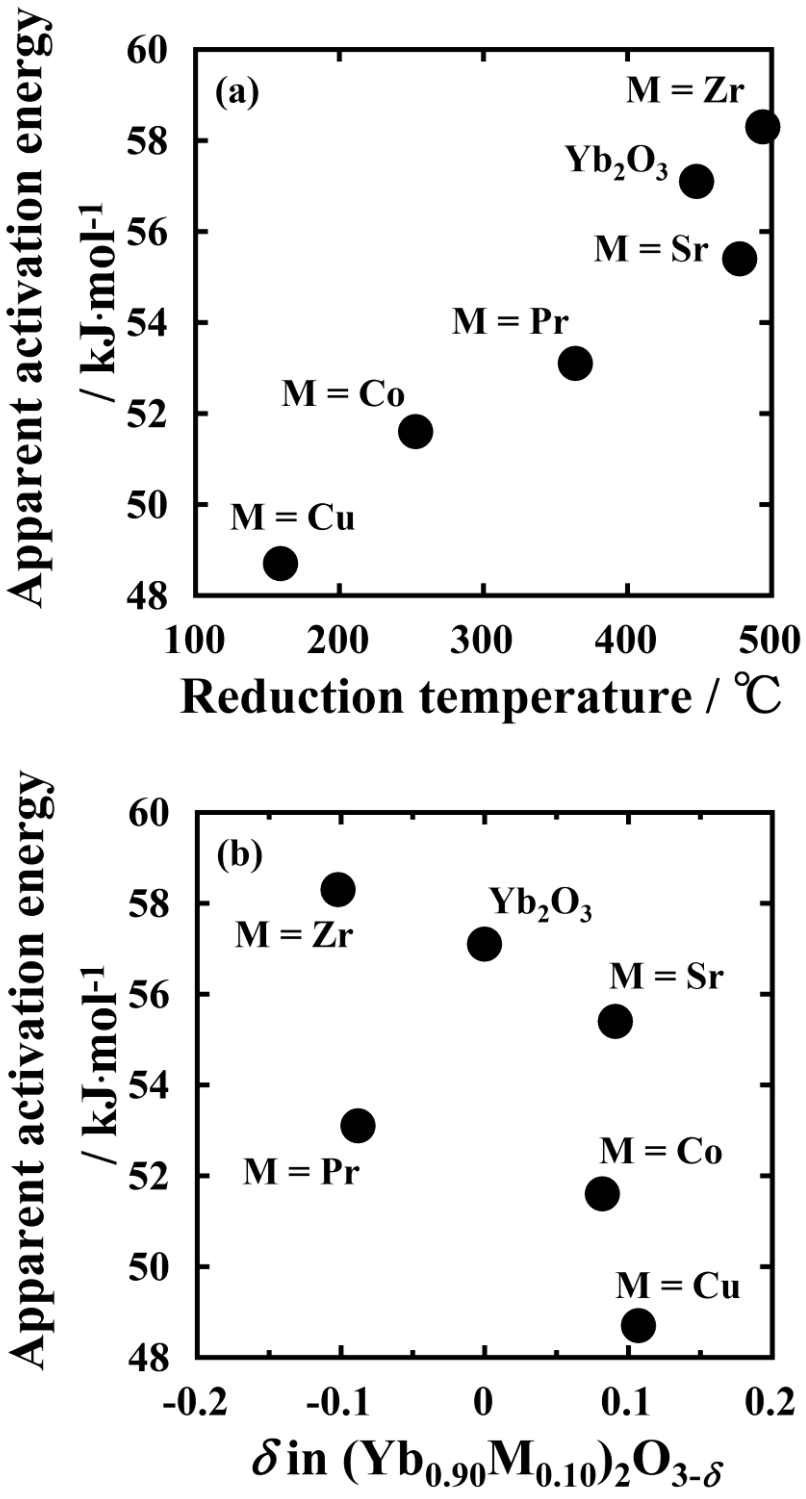

Figure 3-7 Relationship between the apparent activation energy for the N_2O decomposition and (a) the reduction temperature, (b) the amount of oxide ion vacancy, δ.

3.4. Conclusions

In order to investigate the effects of the redox property and the oxide ion vacancy on the N_2O decomposition activity, $(Yb_{0.90}M_{0.10})_2O_{3-\delta}$ (M = Pr, Co, Cu, Sr, Zr) were prepared and their catalytic activities were compared. The introduction of lower valent $Co^{2+/3+}$, $Cu^{+/2+}$, or Sr^{2+} ions into the Yb^{3+} sites caused the formation of oxide ion vacancies. In the case for the doping of $Pr^{3+/4+}$ or Zr^{4+} ion having higher valence number than Yb^{3+}, the excess oxide ions were found to locate at the additional oxygen site (16*c*) in the C-type structure from the Rietveld analysis.

From the relationship between catalytic activity and the amount of oxide ion vacancy (δ), it was clear that the N_2O adsorption amount was influenced by the amount of oxide ion vacancy, suggesting that these vacancies worked as the N_2O adsorption sites.

By the TPR measurement, the order of the redox property of the samples was cleared: $(Yb_{0.90}Cu_{0.10})_2O_{3-\delta}$ > $(Yb_{0.90}Co_{0.10})_2O_{3-\delta}$ > $(Yb_{0.90}Pr_{0.10})_2O_{3-\delta}$ > Yb_2O_3 ≳ $(Yb_{0.90}Sr_{0.10})_2O_{3-\delta}$ ≳ $(Yb_{0.90}Zr_{0.10})_2O_{3-\delta}$, and the redox properties of the samples, which is caused by the valence change of $Cu^{+/2+}$, $Co^{2+/3+}$, and $Pr^{3+/4+}$ ions obviously improved N_2O decomposition activity. Therefore, it can be concluded that both the redox property and the oxide ion vacancy affected the catalytic activity for the direct N_2O decomposition and that the doping of transition metal cations having lower valence such as $Cu^{+/2+}$ is effective for improving the N_2O decomposition activity.

Summary

In this thesis, novel catalysts based on rare earth sesquioxide with cubic C-type structure were developed for the direct nitrous oxide (N_2O) decomposition. Furthermore, the effects of the oxide ion vacancy and the redox property of the C-type rare earth oxide-based catalyst on the catalytic activity were investigated. The results obtained through this study are summarized as follows:

Chapter 1

The N_2O decomposition activity for the cubic C-type R_2O_3 (R = Y, Eu, Gd, Dy, Ho, Er, Tm, Yb, and Lu) were investigated, and it was cleared that Yb_2O_3 exhibited the highest catalytic activity among the C-type R_2O_3 (R = Y, Eu, Gd, Dy, Ho, Er, Tm, Yb, and Lu) solids. Furthermore, the Yb_2O_3 based solids doped with Pr_6O_{11} or Co_3O_4 showed high catalytic activity due to the redox property and the formation of oxide ion vacancy. Both the $(Yb_{0.90}Co_{0.10})_2O_{3-\delta}$ and $(Yb_{0.85}Pr_{0.15})_2O_{3+\delta}$ catalysts, which are the optimum composition for N_2O decomposition, can decompose N_2O into nitrogen and oxygen gases at temperature as low as 500 °C even in the presence of O_2, CO_2, or H_2O, and the $(Yb_{0.90}Co_{0.10})_2O_{3-\delta}$ catalyst showed the higher activity than the $(Yb_{0.85}Pr_{0.15})_2O_{3+\delta}$ case.

Chapter 2

To clarify the effect of the oxide ion vacancy on the direct N_2O decomposition activity, the catalytic activities of the ZrO_2-Y_2O_3 solid solutions, which can hold different types of structure according to the cationic ratio, were investigated. With increasing the oxide ion vacancies (δ) in the $Zr_{1-x}Y_xO_{2-\delta}$ solid solution, the catalytic activity was improved as well as increase of the amount of adsorbed N_2O, and it was found that the C-type structure which can hold a high amount of oxide ion vacancy in its structure showed high catalytic activity. From this result, the effect of oxide ion vacancy

in the C-type structure was revealed; they work as the N_2O adsorption sites and the catalytic active sites.

Chapter 3

In order to investigate the effects of the redox property and the oxide ion vacancy of the C-type rare earth oxide-based catalysts on the N_2O decomposition activity, the various solids, Yb_2O_3-MO_x (M = Pr, Co, Cu, Sr, Zr), were prepared and their activities were compared. The introduction of lower valent $Co^{2+/3+}$, $Cu^{+/2+}$, or Sr^{2+} ions into the Yb^{3+} sites caused the formation of oxide ion vacancies. On the other hand, the introduction of $Pr^{3+/4+}$ or Zr^{4+} ions into the Yb_2O_3 generated the additional oxygen site in the C-type structure. From the discussion on the relationship between apparent activation energy for N_2O decomposition, redox property, and amount of oxide ion vacancy, both the redox property and the oxide ion vacancy contributed to enhance the N_2O decomposition activity. Since the highest activity was obtained for the $Cu^{+/2+}$ doped Yb_2O_3 solid, it can be concluded that the doping of cations having few kinds of lower valence state such as $Cu^{+/2+}$ is effective for the improvement of the direct N_2O decomposition.

References

[1] C. Tricot, A. Berger, *Clim. Dyn.* **1987**, *2*, 39.

[2] M. Konsolakis, *ACS Catal*. **2015**, *5*, 6397.

[3] X. Zhang, Q. Shen, C. He, C. Ma, J. Cheng, L. Li, Z. Hao, *ACS Catal*. **2012**, *2*, 512.

[4] P. J. Smeets, Q. Meng, S. Corthals, H. Leeman, R. A. Shoonheydt, *Appl. Catal. B: Environ*. **2008**, *84*, 505.

[5] J. Pérez-Ramírez, F. Kapteijn, K. Schöffel, J. A. Moulijn, *Appl. Catal. B: Environ*. **2003**, *44*, 117.

[6] L. Matějová, M. Šihor, J. Lang, I. Troppová, N. Ambrožová, M. Reli, T. Brunátová, L. Čapek, A. Kotarba, K. Kočí, *J. Sol-Gel Sci. Technol*. **2017**, *84*, 158.

[7] M. Galle, D. W. Agar, O. Watzenberger, *Chem. Eng. Sci*. **2001**, *56*, 1587.

[8] M. Hussain, D. Fino, N. Russo, *J. Hazard. Mater*. **2012**, *211-212*, 255.

[9] J. Haber, T. Machej, J. Janas, M. Nattich, *Catal. Today* **2004**, *90*, 15.

[10] J. A. Z. Pieterse, S. Booneveld, R. W. Brink, *Appl. Catal. B: Environ*. **2004**, *51*, 215.

[11] J. Pérez-Ramírez, F. Kapteijn, G. Mul, J. A. Moulijn, *Chem. Commun*. **2001**, *8*, 693.

[12] F. Kapteijn, J. Rodriguez-Mirasol, J. A. Moulijn, *Appl. Catal. B: Environ*. **1996**, *9*, 25.

[13] S. Tuti, F. Pepe, D. Pietrogiacomi, V. Indovina, *React. Kinet. Catal. Lett*. **2001**, *72*, 35.

[14] M. F. Fellah, I. Onal, Catal. Today, **2008**, *137*, 410.

[15] R. Amrousse, A. Tsutsumi, A. Bachar, D. Lahcene, *Appl. Catal. A: Gen.* **2013**, *450*, 253.

[16] S. Wójcik, G. Grzybek, J. Gryboś, A. Kotarba, Z. Sojka, *Catal. Commun.* **2018**, *110*, 64.

[17] B. M. Abu-Zied, S. A. Soliman, S. E. Abdellah, *J. Ind. Eng. Chem*. **2015**, *21*, 814.

[18] N. Russo, D. Mescia, D. Fino, G. Saracco, V. Specchia, *Ind. Eng. Chem. Res*. **2007**, *46*, 4226.

[19] K. L. Pan, S. J. Yu, S. Y. Yan, M. B. Chang, *J. Air Waste Manage. Assoc*. **2014**, *64*, 1260.

[20] S. Alini, F. Basile, S. Blasioli, C. Rinaldi, A. Vaccari, *Appl. Catal. B*: *Environ*. **2007**, *70*, 323.

[21] U. Chellam, Z. P. Xu, H. C. Zeng, *Chem*. *Mater*. **2000**, *12*, 650.

[22] Q. Shen, L. Li, J. Li, H. Tian, Z. Hao, *J*. *Hazard*. *Mater*. **2009**, *163*, 1332.

[23] M. Tursun, X. Wang, F. Zhang, H. Yu, *Catal*. *Commun*. **2015**, *65*, 1.

[24] F. Izumi, K. Momma, *Solid State Phenom.* **2007**, *130*, 15.

[25] E. J. Karlsen, M.A. Nygren, L.G.M. Pettersson, *J. Phys*. *Chem*. *A* **2002**, *106*, 7868.

[26] G. Adachi and N. Imanaka, *Chem. Rev.*, **1998**, *98*, 1479.

[27] R. D. Shannon, *Acta Crystallogr*., *Sect. A*. **1976**, *5*, 751.

[28] L. Yan, T. Ren, X. Wang, Q. Gao, D. Ji, J. Suo, *Catal*. *Commun*. **2003**, *4*, 505.

[29] H. Masaki, T. Masui, N. Imanaka, *J*. *Alloy*. *Compd*., **2008**, *451*, 406.

[30] R. G. Reddy, S. G. Kumar, *Metall*. *Mater*. *Trans B*. **1994**, *25B*, 91.

[31] P. Duran, M. Gonzalez, C. Moure, J. R. Jurado, C. Pascual, *J*. *Mater*. *Sci*. **1990**, *25*, 91.

[32] L. Chen, H. Y. Chen, J. Lin, K. L. Tan, *Surf*. *Interface Anal*. **1999**, *28*, 115.

[33] S. S. Kim, S. J. Lee, S. C. Hong, *Chem. Eng. J.* **2011**, *69*, 173.

[34] F. Izumi, K. Momma, *Solid State Phenom.* **2007**, *130*, 15.

[35] Y. Ohno, *J*. *Electron Spectrosc*. *Relat*. *Phenom.* **2008**, *165*, 1.

[36] L. Fan, K. Xi, Y. Zhou, Q. Zhu, Y. Chen, H. Lu, *RSC Adv*., **2017**, *7*, 20309.

[37] L. Xue, C. Zhang, H. He, Y. Teraoka, *Appl. Catal. B: Environ*. **2007**, *75*, 167.

[38] M. F. Luo, Y. J. Zhong, X. X. Yuan, X. M. Zheng, *Appl*. *Catal*. *A: Gen*. **1997**, *162*, 121.

Acknowledgments

The author would like to express his heartfelt gratitude to Professor Dr. Nobuhito Imanaka, Department of Applied Chemistry, Graduate School of Engineering, Osaka University, for his continuous guidance, invaluable suggestions, and science encouragement throughout the work.

The author is very grateful to Dr. Naoyoshi Nunotani, Department of Applied Chemistry, Graduate School of Engineering, Osaka University, for his continuous guidance and stimulating discussion for carrying out this work. The author is also indebted to Dr. Shinji Tamura, Department of Applied Chemistry, Graduate School of Engineering, Osaka University, for his helpful suggestions and apposite advice.

The author obliged to Dr. Yasuyuki Kobayashi, Osaka Research Institute of Industrial Science and Technology, and Dr. Hirokazu Izumi and Dr. Masafumi Fukuzumi, Hyogo Prefectural Institute of Technology, for XPS measurements.

The author is deeply grateful to Professor Dr. Susumu Kuwabata, and Professor Dr. Akinori Saeki, Department of Applied Chemistry, Graduate School of Engineering, Osaka University, for reviewing this thesis and giving their valuable comments.

Special thanks should give to author's co-workers, Ms. Yuka Watanabe, Mr. Naoki Moriyama, Mr. Abdul Rohman Supandi, Mr. Muhammad Radzi Iqbal Bin Misran, Mr. Kenji Matsuo, Mr. Hiroaki Shirai, Mr. Masanari Takashima, Ms. Marina Taira, Mr. Shota Yamauchi, Mr. Takuya Morioki, Mr. Shohei Saeki, Mr. Kentaro Yamada, Mr. Koki Yoshikawa, and the other members of the research group under direction of Professor Dr. Nobuhito Imanaka, Osaka University for their helpful assistance and support in the course of this work.

Finally, the author would like to extend deep gratitude to his parents, Mr. Su-je Cho, and Mrs. Boon-nam Kwon, his sister, Dr. Kyeong-jin Jo, and all members of his family for their encouragement, continuous understanding, and perpetual supports.